Direct Computational Simulations for Internal Condensing Flows and Results on Attainability/Stability of Steady Solutions, Their Intrinsic Waviness, and Their Noise Sensitivity

A. Narain[1]
Mem. ASME
e-mail: narain@mtu.edu

Q. Liang

G. Yu

X. Wang

Department of Mechanical Engineering–Engineering Mechanics, Michigan Technological University, 1400 Townsend Drive, Houghton, MI 49931

The paper presents a new two-dimensional computational approach and results for laminar/laminar internal condensing flows. Accurate numerical solutions of the full governing equations are presented for steady and unsteady film condensation flows on a sidewall inside a vertical channel. It is found that exit conditions and noise sensitivity are important. Even for stable steady solutions obtained for nearly incompressible vapor phase flows associated with unconstrained exit conditions, the noise sensitivity to the condensing surface's minuscule transverse vibrations is high. The structure of waves, the underlying characteristics, and the "growth/damping rates" for the disturbances are discussed. A resonance condition for high "growth rates" is proposed and its efficacy in significantly enhancing wave motion and heat transfer rates is computationally demonstrated. For the unconstrained exit cases, the results make possible a separately reported study of the effects of shear, gravity, and surface tension on noise sensitive stable solutions. [DOI: 10.1115/1.1641063]

1 Introduction

Accurate numerical solutions of the full governing equations are presented for steady and unsteady laminar/laminar film condensation flows on a sidewall inside a vertical channel. This is also a good geometry for addressing (see Liang et al. [1] and Liang [2]) the influence of shear over gravity—either by changing the channel inclination from vertical to horizontal (see Fig. 1) or by studying the flow in the absence of gravity (space applications). Such results are important in understanding qualitative phenomena and obtaining quantitative results (after suitable experimental validations of the computational tool for quasi-steady annular/stratified internal condensing flows) that are relevant to good design and performance of condensers in applications (see Krotiuk [3] and Faghri [4]) such as looped heat pipes, capillary pumped loops, thermal management systems, and electronic-cooling devices. These applications often involve pure vapors with none to negligible presence of noncondensable gases. Fundamental results reported in this paper address issues of annular/stratified condensing flows' heat transfer rates, flow realizability, stability, resonant and nonresonant noise sensitivity, and exit condition sensitivity.

This channel flow geometry is also a simple modification of the classical flat plate geometry associated with classical *external* film condensation flow studies over vertical, horizontal, and tilted walls (Nusselt [5], Rohsenow [6], Sparrow and Gregg [7], Koh et al. [8], Dhir and Lienhard [9], Rose [10], Tanasawa [11], Cess [12], Koh [13], etc.). Heat transfer correlations for laminar and wavy condensate situations for the vertical/inclined plate geometry are given by Kutateladze [14] and correlations for turbulent condensate, as proposed by Labuntsov [15], are given in Incropera and DeWitt [16]. For smooth-interface laminar/laminar condensing flows over a flat plate in vertical, horizontal, and tilted configurations; the computational approach developed in this paper yields results (see Yu [17]) in agreement with the relevant solutions of Nusselt [5] and Koh [14].

With regard to *internal* condensing flows, some qualitative understanding exists in papers by Chow and Parish [18], Narain et al. [19], etc. These analyses/predictions rely on integral control volume formulations that employ *models* for interfacial shear (e.g., Henstock and Hanratty [20]) and are typically available only for fast vapor motions requiring no exit condition specification (i.e., the vapor flow in Fig. 1 is ''parabolic''). To address laminar/laminar flow issues that cannot be addressed by the above approach, direct numerical simulations are undertaken here to better understand the wave phenomena and associated effects. Strictly speaking the results presented here are valid only for laminar vapor flows (i.e., inlet vapor Reynolds number based on channel height as characteristic length should be approximately less than 1400–2000) and laminar condensate flows (i.e., film Reynolds number as defined in Incropera and DeWitt [16] should be approximately less than 1400–1800). In practice, inlet vapor Reynolds number up to 7000 is allowed because of sufficiently thick laminar sub-layer in the vicinity of the interface. This is because vapor streamlines, as they approach the interface, are almost perpendicular to it (see Liang et al. [1]) and the velocity along the streamlines are very small. This allows the vapor streamlines to pierce the interface and drift downstream as liquid streamlines in an even slower motion of the *laminar* condensate. As a result, it is found that computational predictions of film thickness, heat transfer rates, etc. under laminar/laminar assumptions (though perhaps

[1]To whom correspondence should be addressed.

Contributed by the Applied Mechanics Division of THE AMERICAN SOCIETY OF MECHANICAL ENGINEERS for publication in the ASME JOURNAL OF APPLIED MECHANICS. Manuscript received by the Applied Mechanics Division, December 12, 2002; final revision, June 9, 2003. Associate Editor: T. E. Tezduyar. Discussion on the paper should be addressed to the Editor, Prof. Robert M. McMeeking, Journal of Applied Mechanics, Department of Mechanical and Environmental Engineering, University of California–Santa Barbara, Santa Barbara, CA 93106-5070, and will be accepted until four months after final publication of this paper in the ASME JOURNAL OF APPLIED MECHANICS.

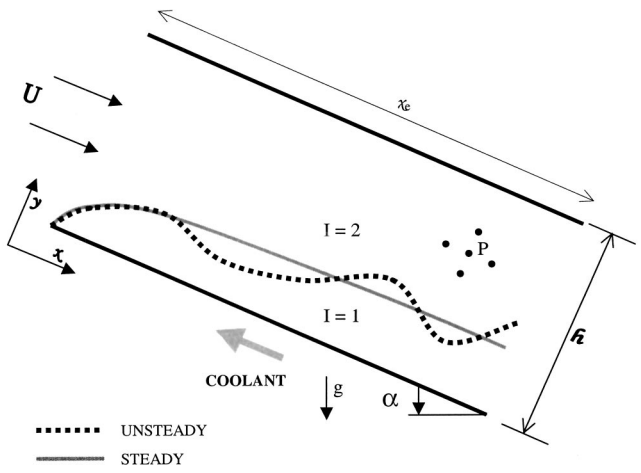

Fig. 1 Flow geometry for simulations

not the predictions of vapor velocity profile outside the laminar sublayer of the vapor surrounding the interface!) are in good agreement (see Liang et al. [1]) up to inlet Reynolds number as high as 8000, with relevant experimental results of Lu [21].

This paper proposes a novel and direct computational technique for steady and unsteady internal condensing flows in the annular/stratified regime. The unsteady laminar/laminar simulations employ a suitable adaptive grid and numerical solution of the appropriate hyperbolic *interface tracking equation* which is the same as the one used in level-set method (see Sussman et al. [22] and Son and Dhir [23]), VOF method (see Hirt and Nichols [24]), and other methods (Tezduyar [25], etc.). The numerical scheme used in this paper for the *interface tracking equation* exploits existing mathematical knowledge and experience for this equation (see Abbott and Basco [26]) to sidetrack the inaccuracy problems associated with reconstructing interface location within and around the *interface cells* predicted by VOF or related interface *capturing* techniques (see Tezduyar [25], Li and Renardy [27], etc.). The scheme used here ensures convergence and accuracy of both the amplitude and the phase of the interfacial waves. At each time step, the scheme locates the interface, solves the Navier-Stokes equation in each phase, satisfies the full nonlinear conditions at the phase-change interface, and satisfies the relevant inlet, outlet, and wall conditions. Since vapor in internal condensing flows slow down by the exit, the steady vapor flow equations are ''elliptic'' in the exit region (i.e., downstream points affect a flow variable's value at a representative point P in Fig. 1) and exit condition needs to be specified for a solution. Note that any condenser section of the type shown in Fig. 1 is, typically, just a *part* of a flow loop. A flow loop which maintains a constant pressure p_0 and constant flow rate of saturated vapor at the inlet may also be designed (see, e.g., Fig. 2) to provide: (a) an unconstrained exit condition (which is very often the case when exit pressure, or equivalently, exit vapor flow rate is free to adjust to any value it seeks) that allows the vapor to flow at nearly constant density (its density at the inlet), or (b) a constrained exit condition (this situation arises, when further downstream of the exit, there are natural constraints in the flow loop or, as in Fig. 2, there are active flow control devices) that forces non-negligible vapor density variations between the inlet and the outlet of the condenser section. For the constrained exit case not considered in this paper, the ''unsteady'' equations are also spatially ''elliptic'' near the exit and an exit condition can be prescribed if a nonconstant vapor density and an equation of state—of the type $\rho_2=\rho_2(p_2,\mathcal{T}_2)$— is incor-

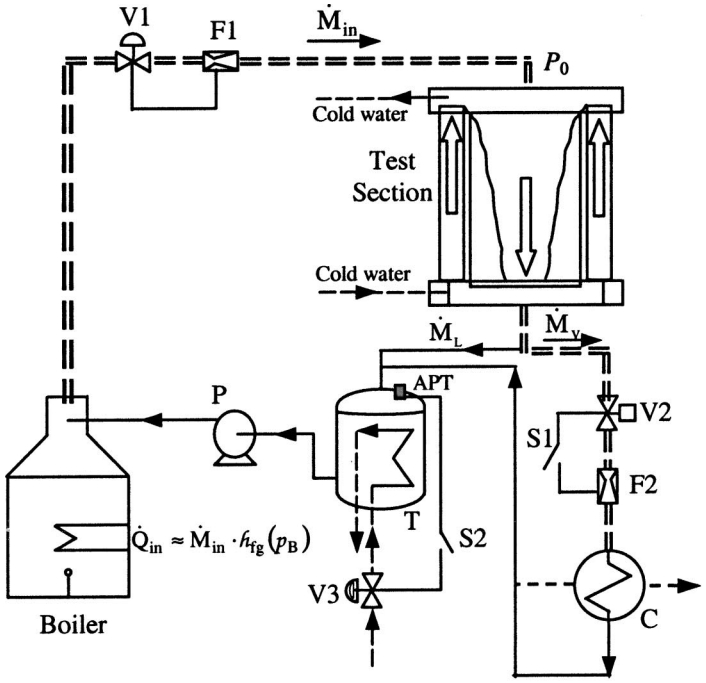

V1, V2: Solenoid Valve
V3: Pneumatic Valve
F1, F2: Flow Meter
S1, S2: Switch
P: Variable Head Pump
T: Sub cooled Tank
C: Auxiliary Condenser
APT: Absolute Pressure Transducer

Unconstrained Exit:
With fixed pressure and flow rate at the inlet of the test-section, valve V2 and pressure in T are not actively controlled (S1 and S2 open) and steady state is naturally achieved with tank T completely filled with liquid. The system finds natural values of exit vapor quality $Z_e = Z_e|_{Na}$ and pressure at APT.

Constrained Exit:
With fixed pressure and flow rate at the inlet of the test-section, valve V2 is controlled to a set point value in F2 while the pressure at APT in a partially filled T is held fixed at a value lower than its natural value for the unconstrained case. The flow can now be steady/quasi-steady at different exit vapor qualities (including $Z_e \neq Z_e|_{Na}$).

Fig. 2 The solenoid valve *V*1 (actively controlled by flow meter *F*1) and constant heat input $\dot{Q}_{in} \approx \dot{M}_{in} \cdot h_{fg}(p_B)$ to the boiler fixes inlet pressure p_0 and inlet flow rate to the test section. The mass flow rate through pump *P* is adjusted to a value that matches the corresponding value at *F*1. A high flow rate of the coolant (water) flow around the test section fixes condensing surface temperature at a nearly uniform value of $\mathcal{T}_w$ while it still allows for different heat removed rates for different exit qualities Z_e.

porated in the governing equations for the vapor phase. The unconstrained exit case, for which vapor compressibility is unimportant, is the focus of steady and unsteady simulations in this paper. For these simulations the ''unsteady'' equations for the unconstrained exit case are *not* spatially ''elliptic'' and an exit condition cannot be prescribed if a constant inlet vapor density $\rho_2=\rho_{20}$ is assumed in the governing equations. Constant vapor density assumption is valid for conditions involving $\Delta\rho_2/\rho_{20}\ll 1$ or, say, $\Delta\rho_2/\rho_{20}$ is less than 5% —this being the typical criteria for assuming incompressibility for gases that flow inside a duct and have Mach number values less than 0.3. For the unconstrained exit cases involving an assumed constant density for the vapor phase, it is shown in this paper that, if at $t=0$, one starts at *any* steady solution of the steady ''elliptic'' problem in Fig. 1 (under *any* reasonable and well-defined exit condition), then, over time (utilizing unconstrained unsteady simulation for $t\geqslant 0$), a natural steady solution and an associated natural exit condition is obtained at large times. This naturally determined value of the exit condition for prescribed inlet condition is very similar to the well-known behavior of other incompressible duct flows (single phase or air/water flows) which also exhibit well-defined pressure difference for given inlet pressure and flow rate. In fact, in Liang et al. [1], it is shown that the naturally selected quasi-steady computational solutions that are obtained for flow cases considered in the experimental runs of Lu [21] and Lu and Suryanarayana [28] yield values of film thickness, heat transfer rates, etc., that are in good agreement with experimentally obtained values. While this generates confidence in the proposed method of identifying stable steady solutions, these stable solutions are shown here to be sensitive to minuscule bottom plate noise that are typically almost always present. This makes the interface wavy for most situations. The reported determination of phase speeds and *characteristics curves* (along which disturbances propagate) for the waves improve our understanding of these flows and leads to a proposal of a new hitherto unknown resonance condition whose efficacy is also demonstrated in this paper. It is shown that specifically designed noise sources placed at suitably specified locations and specified variations in frequency satisfy the resonance criteria and enhance the wave energy and heat transfer rates significantly.

Unsteady simulations starting from steady solutions for the constrained exit cases are not considered here. In this case, compressibility effects on the stability and noise-sensitivity are expected to be important and these effects are one of the underlying causes behind various interesting experimental results (see Bhatt et al. [29], etc.) dealing with experiments whose exit conditions are constrained. The stability and flow oscillations issues associated with this case are also believed to arise in applications such as Looped Heat Pipes (Faghri [4]) where limits on the power of passive pumping (wicks, etc.) cause pressure variation constraints at the condenser exit while approximately constant values of pressure and flow rate is retained at the condenser inlet.

This paper restricts itself to consideration of single but arbitrary Fourier components of bottom plate noise (standing waves) and avoids discussions of wave interactions resulting from more complex random noises made up of several Fourier components. Within this limited context, we find that the front-steepening solitary wave patterns that are experimentally observed on air/water type vertical liquid films (see Liu and Gollub [30] and Alekseenko, et al. [31]) or the ones that are obtained by Miyara [32] in the reported computational simulations for the Nusslet [5] problem that deals with condensation on a vertical plate, occur much more gradually for the gravity dominated internal condensing flow cases considered here. Categorization of *typical noise levels* (with a random mix of amplitude, frequency, and wavelengths) and *typical responses* (or *strange attractors* as termed by Liu and Gollub [30]) requires separate study and is outside the scope of this paper. Furthermore, unlike gravity driven shallow or deep water waves (see Lighthill [33]), the reported waves, in their linearized limits, are nondispersive (i.e., phase speeds do not depend on the frequency or wavelengths of the disturbance). For the above reasons, neither a survey of results nor comparisons with results from the vast literature on noncondensing air/water type film flows (Alekseenko et al. [31]) is considered to be within the scope of this paper.

The results presented here underscore the importance of including the role of exit conditions and noise sensitivity in categorizing heat transfer correlations and flow regime maps. Therefore currently available heat transfer correlations (Traviss et al. [34]; Shah [35]; etc.) and flow regime maps (see Hewitt et al. [36], Carey [37], etc.) can be improved to address their reported deficiencies (see Palen et al. [38]). Therefore the reported results on exit conditions, noise sensitivity, and flow regime boundaries—in conjunction with proper experiments and use of computational tool such as the one proposed here—will eventually be of value in better categorization and development of relevant heat-transfer correlations and flow regime maps.

2 Governing Equations

The liquid and vapor phases in the flow (e.g., see Fig. 1) are denoted by a subscript I: $I=1$ for liquid and $I=2$ for vapor. The fluid properties (density ρ, viscosity μ, specific heat C_p, and thermal conductivity k) with subscript I are assumed to take their representative constant values for each phase ($I=1$ or 2). Let $\mathcal{T}_I$ be the temperature fields, p_I be the pressure fields, $\mathcal{T}_s(p)$ be the saturation temperature of the vapor as a function of local pressure p, Δ be the film thickness, $\dot{m}$ be the local interfacial mass flux, $\mathcal{T}_w$ (x) $(<\mathcal{T}_s(p))$ be a *known* temperature variation of the cooled bottom plate, and $\mathbf{v}_I=u_I\hat{\mathbf{i}}+v_I\hat{\mathbf{j}}$ be the velocity fields. Furthermore, let h be the channel height, g_x and g_y be the components of gravity along x and y-axes, p_0 be the inlet pressure, $\Delta T\equiv\mathcal{T}_s(p_0)-\mathcal{T}_w(0)$ be a representative controlling temperature difference between the vapor and the bottom plate, h_{fg} be the heat of vaporization at temperature $\mathcal{T}_s(p)$, and U be the *average* inlet vapor speed determined by the inlet mass flux. With t representing the actual time and (x, y) representing physical distances of a point with respect to the axes in Fig. 1 ($x=0$ is at the inlet and $y=0$ is at the condensing surface), we introduce a new list of fundamental nondimensional variables—viz. $(x,y,t,\delta,u_I,v_I,\pi_I,\theta_I,\dot{m})$ —through the following definitions:

$$\{x,y,\Delta,u_I,\dot{m}\}\equiv\{h.x,h\cdot y,h\cdot\delta,U\cdot u_I,\rho_I\cdot U\cdot\dot{m}\}$$

$$\{v_I,\mathcal{T}_I,p_I,t\}\equiv\{U\cdot v_I,(\Delta\mathcal{T})\cdot\theta_I,p_0+\rho_I U^2\cdot\pi_I,(h/U)\cdot t\}. \tag{1}$$

Interior Equations. The nondimensional differential forms of mass, momentum (x and y components), and energy equations for incompressible flow in the interior of either of the phases are the well-known equations:

$$\frac{\partial u_I}{\partial x}+\frac{\partial v_I}{\partial y}=0$$

$$\frac{\partial u_I}{\partial t}+u_I\frac{\partial u_I}{\partial x}+v_I\frac{\partial u_I}{\partial y}=-\left(\frac{\partial\pi_I}{\partial x}\right)+\mathrm{Fr}_x^{-1}+\frac{1}{\mathrm{Re}_I}\left(\frac{\partial^2 u_I}{\partial x^2}+\frac{\partial^2 u_I}{\partial y^2}\right)$$

$$\frac{\partial v_I}{\partial t}+u_I\frac{\partial v_I}{\partial x}+v_I\frac{\partial v_I}{\partial y}=-\left(\frac{\partial\pi_I}{\partial y}\right)+\mathrm{Fr}_y^{-1}+\frac{1}{\mathrm{Re}_I}\left(\frac{\partial^2 v_I}{\partial x^2}+\frac{\partial^2 v_I}{\partial y^2}\right)$$

$$\frac{\partial\theta_I}{\partial t}+u_I\frac{\partial\theta_I}{\partial x}+v_I\frac{\partial\theta_I}{\partial y}\approx\frac{1}{\mathrm{Re}_I\,\mathrm{Pr}_I}\left(\frac{\partial^2\theta_I}{\partial x^2}+\frac{\partial^2\theta_I}{\partial y^2}\right), \tag{2}$$

where $\mathrm{Re}_I\equiv\rho_I Uh/\mu_I$, $\mathrm{Pr}_I\equiv\mu_I C_{pI}/k_I$, $\mathrm{Fr}_x^{-1}\equiv g_x h/U^2$ and $\mathrm{Fr}_y^{-1}\equiv g_y h/U^2$.

Interface Conditions. The nearly exact interface conditions (see Delhaye [39], etc.) for condensing flows are given in the Appendix (see Eqs. (*A*1)–(*A*8)). Utilizing a superscript "*i*" for values of flow variables at the interface $\mathcal{H}=y-\Delta(x,t)=0$, nondimensional forms of the interface conditions in the Appendix are as given below.

- The nondimensional form of the requirement of continuity of tangential component of velocities, as given by Eq. (*A*2), becomes
$$u_2^i = u_1^i - \delta_x (v_2^i - v_1^i), \tag{3}$$
where $\delta_x \equiv \partial\delta/\partial x$.
- The nondimensional form of the normal component of momentum balance at the interface, as given by Eq. (*A*3), becomes
$$\pi_1^i = \frac{\rho_2}{\rho_1}\pi_2^i - \frac{1}{\mathrm{We}}\left(\frac{\delta_{xx}}{[1+\delta_x^2]^{3/2}}\right) + \dot{m}^2\left(\frac{\rho_1}{\rho_2}-1\right), \tag{4}$$
where $\mathrm{We}\equiv\rho_1 U^2 h/\sigma$, and surface tension σ is assumed to be nearly constant because of the nearly constant interface temperature. As reported elsewhere, results for $\sigma=\sigma(\mathcal{T}_s(p_2^i))$ in Eqs. (*A*3)–(*A*4), are nearly the same as the ones reported here for constant σ.
- The tangential component of momentum balance at the interface, as given by Eq. (*A*4), becomes
$$\left.\frac{\partial u_1}{\partial y}\right|^i = \frac{\mu_2}{\mu_1}\left.\frac{\partial u_2}{\partial y}\right|^i + [t], \tag{5}$$
where the term $[t]$ in Eq. (5) is defined in Eq. (*A*9) of the Appendix.
- The nondimensional form of mass fluxes $\dot{m}_{LK}$ and $\dot{m}_{VK}$ in Eq. (*A*5) become
$$\dot{m}_{LK} \equiv [u_1^i(\partial\delta/\partial x) - (v_1^i - \partial\delta/\partial t)]/\sqrt{1+(\partial\delta/\partial x)^2}, \quad \text{and}$$
$$\dot{m}_{VK} \equiv (\rho_2/\rho_1)[u_2^i(\partial\delta/\partial x) - (v_2^i - \partial\delta/\partial t)]/\sqrt{1+(\partial\delta/\partial x)^2} \tag{6}$$
- The nondimensional form of $\dot{m}_{\mathrm{Energy}}$ in Eq. (*A*6) becomes
$$\dot{m}_{\mathrm{Energy}} \equiv \mathrm{Ja}/(\mathrm{Re}_1\,\mathrm{Pr}_1)\{\partial\theta_1/\partial n|^i - (k_2/k_1)\partial\theta_2/\partial n|^i\}, \tag{7}$$
where $\mathrm{Ja}\equiv C_{p1}\Delta T/h_{fg}^0$, and $h_{fg}^0 \equiv h_{fg}(\mathcal{T}_s(p_o))$.
- Nondimensional form of interfacial mass balance in Eq. (*A*7) becomes
$$\dot{m}_{LK} = \dot{m}_{VK} = \dot{m}_{\mathrm{Energy}} \equiv \dot{m}. \tag{8}$$
- The nondimensional thermodynamic restriction on interfacial temperatures, as given by Eq. (*A*8), becomes
$$\theta_1^i \cong \theta_2^i = \mathcal{T}_s(p_2^i)/\Delta\mathcal{T} \equiv \theta_s(\pi_2^i). \tag{9}$$

Within the vapor phase, for the refrigerants considered here, changes in absolute pressure relative to the inlet pressure are typically small to affect temperatures. Therefore $\theta_s(\pi_2^i)\cong\theta_s(0)$.

Boundary Conditions. The problem posed by Eqs. (2)–(9) are computationally solved subject to boundary conditions that are

- at the inlet ($x=0, 0\leqslant y\leqslant 1$) at any time *t*:
$$u_2(0,y,t)=1 \quad v_2(0,y,t)=0$$
$$\pi_2(0,y,t)=0 \quad \theta_2(0,y,t)=\theta_s(0). \tag{10}$$
- at the bottom wall ($y=0, 0\leqslant x\leqslant x_e$) at any time *t*:
$$u_1(x,0,t)=0, \quad v_1(x,0,t)=0, \quad \theta_1(x,0,t)=\theta_w, \tag{11}$$
where $\theta_w\equiv\mathcal{T}_w(x)/\Delta\mathcal{T}$ is a constant unless it is otherwise specified. In case of flow in Fig. 2, this situation arises whenever, for a given heat load, the coolant flow rate is high enough to make the coolant its temperature rise negligible as it flows past the test section.
- at the top wall ($y=1, 0\leqslant x\leqslant x_e$) at any time *t*:
$$u_2(x,1,t)=0, \quad v(x,l,t)=0, \quad \theta_2(x,1,t)=\theta_s(0). \tag{12}$$

Furthermore, because of the nature of boundary conditions in Eqs. (10)–(12), $\theta_2(x,y,t)\cong\theta_s(0)$ is assumed/prescribed to limit the discussions in this paper to the flow of saturated vapor. This is done because, for the *pure* vapor flows considered here, it is easy to verify the well-known fact that the effects of superheat (commonly in the 5–10°C range) are negligible.

Exit Conditions. Any condenser section of the type shown in Fig. 1 is typically a *part* of a closed flow loop. A flow loop (see, e.g., Fig. 2), which maintains a constant flow rate and constant pressure p_o (i.e. $\pi_2=0$) at the inlet, may also be designed to provide: (a) an unconstrained exit condition (which is very often the case), or (b) a constrained exit condition (this may arise from downstream constraints in the flow loop or active flow control of the downstream flow). An exit condition, at any time *t*, is specified by either specifying the value of the average cross-sectional pressure of the vapor at the exit or, equivalently (as seen later from results such as the one in Fig. 6), by specifying the exit vapor quality $Z_e(t)$. Exit vapor quality $Z_e(t)$ is the ratio of vapor mass flow rate at exit ($x=x_e$) to vapor mass flow rate at inlet.

For the case of *constrained* exit conditions, vapor compressibility effects cannot be ignored for unsteady simulations, and hence one cannot treat vapor density $\rho_2(x,y,t)$ to be a constant equal to its inlet value ρ_{20}. For these compressible cases, the "elliptic" equations for the vapor would require specification of the exit vapor quality $Z_e(t)$ defined as
$$Z_e(t) = \int_{\delta(x_e,t)}^{1} \{\rho_2(x_e,y,t)/\rho_{20}\} u_2(x_e,y,t)\cdot dy, \tag{13}$$
while allowing for nonconstant unsteady/steady vapor density values. This constrained exit case, though important in some cases because of the interesting compressibility effects on flow stability and noise sensitivity (see Bhatt et al. [27], etc.), is not considered here.

For the "elliptic" steady cases considered here for $t\leqslant 0$, the vapor density is assumed to be a constant with $\rho_2=\rho_{20}$ and exit condition is specified here by assigning a fixed value for the exit vapor quality Z_e given by
$$Z_e = \int_{\delta_{\mathrm{steady}}(x_e)}^{1} u_{2\,\mathrm{steady}}(x_e,y)\cdot dy. \tag{14}$$

For unsteady cases under the assumption of constant vapor densities $\rho_2(x,y,t)=\rho_{20}$, the "unsteady" equations are not "elliptic" near the exit and unsteady exit vapor quality $Z_e(t)$ in Eq. (13) cannot be specified.

Initial Conditions. If $t=0$ is chosen to be the time when saturated vapor first comes in contact and condenses on a dry subcooled ($\mathcal{T}_w(x)<\mathcal{T}_s(p_0)$) bottom plate, the above described *continuum* equations do not apply at early times ($t\sim 0$) because they do not model and incorporate relevant intermolecular forces into the governing equations. These intermolecular forces are important in determining the evolution of very thin (approximately over 10–100 nm of film thickness) condensate film $\delta(x,t)$. Because of the above modeling limitations, the strategy here is to start at $t=0$, with *any* sufficiently thick *steady* solution of the *continuum* equations where all the governing equations clearly apply. That is, if $\phi(x,y,t)$ is any variable (such as u_I, v_I, π_I, θ_I, etc.), the initial values of ϕ and film thickness $\delta(x,t)$ are such that
$$\phi(x,y,0)=\phi_{\mathrm{steady}}(x,y) \quad \text{and} \quad \delta(x,0)=\delta_{\mathrm{steady}}(x), \tag{15}$$
where ϕ_{steady} and δ_{steady} are solutions of the governing equations obtained by dropping all time dependencies in Eqs. (2)–(12) and solving the resulting steady equations (which are *elliptic* near exit) for *any* arbitrarily prescribed value of $Z_e(0)=Z_e$, where Z_e is given by Eq. (14). The prescription of Z_e within $0<Z_e<1$ is

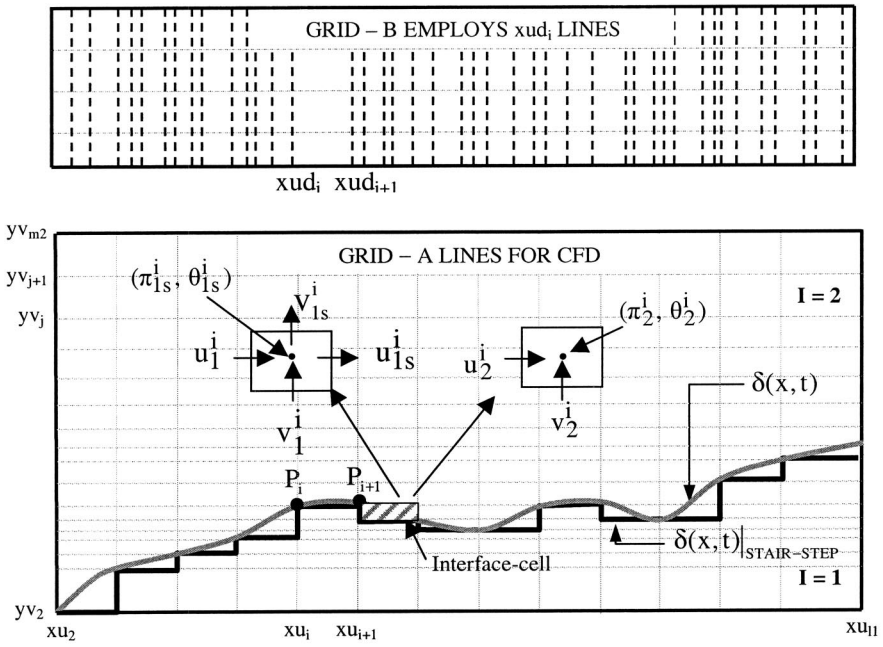

Fig. 3 Computational grids for flow simulation. For chosen xu_i lines, yv_j lines in grid A are first generated by points P_i on $\delta(x,t)$. Above the "highest" yv_j line thus obtained, the remaining yv_j lines are independently generated with suitable unequal spacings. Grid B lines at $x=xud_i$ are different from xu_i lines and are used for tracking the interface $\delta(x,t)$.

arbitrary except that it should be such that it should allow a steady computational solution in the stratified/annular regime indicated in Fig. 1. It is shown later that there exists a naturally selected value of Z_e (denoted as $Z_e|_{\mathrm{Na}}$) which allows the steady solution to be stable and consistent with the chosen constant vapor density.

An inspection of all the non-dimensional governing equations, interface conditions, and boundary conditions reveal the fact that the flows considered here are affected by the following set of nondimensional parameters:

$$\left\{ \mathrm{Re}_{in}, \mathrm{Ja}, \mathrm{Fr}_x^{-1}, \frac{\rho_2}{\rho_1}, \frac{\mu_2}{\mu_1}, \mathrm{Pr}_1, x_e, Z_e(0), \mathrm{We}, \mathrm{Fr}_y^{-1} \right\}, \qquad (16)$$

where $\mathrm{Re}_{in} \equiv \rho_2 U h/\mu_2 \equiv \mathrm{Re}_2$. Here Re_{in}, Fr_x^{-1}, and Ja are control parameters associated with inlet speed U, inclination α, and temperature difference ΔT. For *unconstrained* exit conditions considered here, it is seen later that $Z_e(0)$ is not important because it does not affect the naturally selected steady solution and its associated exit vapor quality $Z_e|_{\mathrm{Na}}$. For *constrained* exit conditions not studied here, e.g., a prescription of time-averaged $Z_e(t) = Z_e(0)$ or $Z_e(t) = Z_e(0)$ for all $t \geqslant 0$, the value of the parameter $Z_e(0)$ becomes important. The density ratio ρ_2/ρ_1, viscosity ratio μ_2/μ_1, and Prandtl number Pr_1 are passive fluid parameters. Also, for unsteady or quasi-steady wavy-interface situations, the above equations imply additional dependences on a surface tension parameter, Weber number $\mathrm{We} \equiv \rho_1 U^2 h/\sigma$, and a transverse gravity parameter $\mathrm{Fr}_y^{-1} \equiv g_y h/U^2$. For superheated vapors, there is a very weak dependence, through Eq. (7), on the thermal conductivity ratio k_2/k_1.

3 Computational Approach for Steady and Unsteady Solutions

For readers not interested in algorithm or code development, only a cursory reading of this section is recommended.

Adaptive Grid and Computational Approach. At each interface configuration, while solving the steady or unsteady problem, the fluid flow computational domains for each phase ($I=1$ or 2) are defined by grid A in Fig. 3. A finite number of discrete points P_i on the interface define a stair-step geometrical approximation for the interface $\delta(x,t)$. Use of this stair-step approximation still allows second-order ($O(\Delta x^2)$ and $O(\Delta t^2)$) accurate physical values of $\delta(x_{\mathrm{P}_i}, t)$ because these values are used to generate higher order approximations to estimate intermediate physical values of $\delta(x,t)$ for discretization of the interface conditions (e.g., piecewise linear approximations for evaluation of the slope terms and cubic splines for evaluation of $\partial^2\delta/\partial x^2$ term appearing in the surface tension term of Eq. (4)). Each interface point P_i, at $x = xu\ (i)$, are marked by a tagging function "$xx\ (i)$" to identify whether the point belongs to an increasing ($xx\ (i)=1$), flat ($xx\ (i)=0$), or decreasing ($xx\ (i)=-1$) section of the interface. These points are also used to generate and define the xu and yv lines that are parallel to the coordinate axes (see Section 4.3 of Liang [2] for details). These lines also form the faces of the rectangular finite volume cells in the interior of each of the two phases.

For the *interiors* of the two fluid phases defined by grid A in Fig. 3, the chosen CFD approach is same as the SIMPLER approach of Patankar [40]. This makes the computations in the interior quite conservative because all balance laws are satisfied even for the coarser control volumes. However, at any time t and location (x, y) where the control volume (say of size $\Delta x_c \times \Delta y_c$) are near the interface cells, the truncation errors $\Delta\delta_T$ and $\Delta\phi_T$ in the discretizations for film thickness δ and any other flow variable ϕ are given by the relations

$$\Delta\varphi_T \approx \sqrt{\Delta\varphi_x^2 + \Delta\varphi_y^2 + \Delta\varphi_t^2} \quad \text{and} \quad \Delta\delta_T \approx \sqrt{\Delta\delta_x^2 + \Delta\delta_t^2}, \qquad (17)$$

where $\Delta\varphi_x \equiv \partial\varphi/\partial x \cdot \Delta x_c$, $\Delta\varphi_y \equiv \partial\varphi/\partial y \cdot \Delta y_c$, $\Delta\varphi_t \equiv \partial\varphi/\partial t \cdot \Delta t_c$, $\Delta\delta_x \equiv \partial^2\delta/\partial x^2 \cdot (\Delta x_c)^2$, and $\Delta\delta_t \equiv \partial^2\delta/\partial t^2 \cdot (\Delta t_c)^2$. The first order accuracy in ϕ above is due to second order discretization of δ and a mixed second-order and first-order discretizations for the remaining terms appearing in the interface conditions.

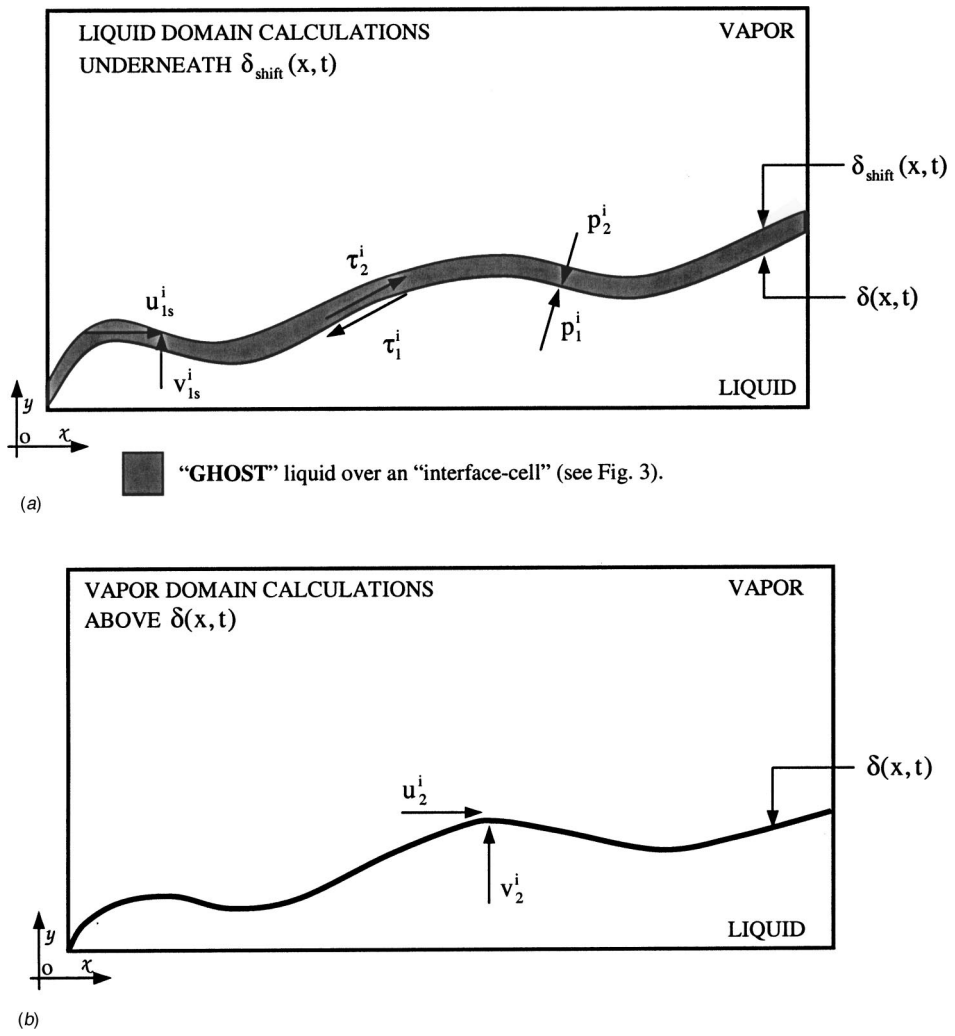

Fig. 4 (*a*) The liquid domain calculations underneath $\delta_{shift}(x,t)$ with prescribed values of $(u_{1s}^i, v_{1s}^i, \theta_{1s}^i)$ on $\delta_{shift}(x,t)$ satisfy the shear and pressure condition on $\delta(x,t)$. (*b*) The vapor domain calculations above $\delta(x,t)$ with prescribed values of $(u_2^i, v_2^i, \theta_2^i)$ on $\delta(x,t)$ satisfy $\dot{m}_{VK} = \dot{m}_{Energy}$ and the requirement of continuity of tangential velocities.

While consistent higher order discretizations of all the interface conditions can enhance accuracy, it is important to recall that the overall discretization errors in the solutions is best estimated by the convergence trends observed during refinement of the grids (see Section 3.10 of Ferziger and Peric [41]). Since the nonuniform grid A is very refined in the *y*-direction near the interface (i.e., small Δy_c^i) and acceptably coarse along the *x*-direction (Δx_c^i), the overall convergence trends (discussed in Section 6) are found to be good without excessive computational penalties in terms of memory and speed requirements (see Liang [2]).

With the help of known inlet and boundary conditions and standard CFD approach for single fluid flows, separate solutions for each domain is easy to obtain provided one has a correct guess of the interface $\delta(x,t)$ and correct values of $\{u_1^i, v_1^i, \theta_1^i\}$ on the interface in Fig. 4(*a*) (or, as depicted in the inset of Fig. 3, on a representative liquid interface cell in grid A), and, also, correct values of $\{u_2^i, v_2^i, \theta_2^i\}$ on the interface in Fig. 4(*b*) (or, as depicted in the inset of Fig. 3, on a representative vapor interface cell in grid A). In reality though, one has to make tentative guesses of these seven variables—viz: $\{u_1^i, v_1^i, \theta_1^i, u_2^i, v_2^i, \theta_2^i, \delta\}$—and then iteratively arrive at their correct values by repeatedly updating them with the help of the interface conditions, vapor domain solutions, and liquid domain solutions. Disregarding the two known and nearly constant temperatures θ_1^i and θ_2^i obtained through Eq. (9), the remaining *five* guesses are updated to their correct values with the help of *five* interface conditions—three from Eqs. (3)–(5) and two from Eq. (8). However, on use of the above described approach for obtaining a steady solution of the ''elliptic'' steady problem, it is found that such steady solutions are not *unique* and many liquid/vapor interface configurations are possible unless a suitable exit condition is specified. That is steady solutions carry the signature of the well-known degeneracy associated with saturated vapor's quality (i.e., any liquid/vapor interference configuration or all vapor or all liquid) under quiescent and equilibrium thermodynamic conditions. To find a unique steady solution, the exit vapor quality Z_e is specified (this is equivalent to specifying exit pressure or the amount of heat removed) and only then a unique solution is obtained (this is accomplished by ''creating' a fictitious interface type condition described later in Eq. (19)). For unsteady simulations, if the exit conditions are unconstrained and the vapor flow is incompressible, one can start from one of these steady solutions at time $t=0$ and ascertain the real time evolution of this solution at $t>0$ without specifying the exit quality $Z_e(t)$. As $t\to\infty$, these unsteady solutions naturally seek out the right exit conditions that are consistent with the assumed constant value of the vapor density. For these unsteady solutions, the five values of

$\{u_1^i, v_1^i, u_2^i, v_2^i, \delta\}$ at any time "$t+\Delta t$" are obtained from the known values of these variables at time "t" and the *five* interface conditions (three from Eqs. (3)–(5) and two from Eq. (8)) discussed earlier. For the constrained exit case not considered in this paper, prescription of the value of $Z_e(t)$ at all times "t" (with the help of an equation of the type given in Eq. (19)) requires nonconstant vapor density ρ_2 and this changes the list of interfacial unknowns to eight: viz. $\{u_1^i, v_1^i, \theta_1^i, u_2^i, v_2^i, \theta_2^i, \delta, \rho_2^i\}$. Again this compressible case becomes solvable with eight conditions (the earlier seven interface conditions plus the eighth condition arising from the specified exit condition) for eight interfacial unknowns that need to be guessed for the unsteady equations governing condensing flows with compressible vapor.

To obtain separate calculations for the vapor domain in Fig. 4(*b*), the temporarily guessed values of $\{u_2^i, v_2^i, \theta_2^i\}$ on the interface are temporarily held fixed along the interface and the entire vapor flow field on grid A of Fig. 3 is obtained with the help of the inlet and the top wall conditions. After obtaining the full solution, the flow field values underneath the interface (the liquid domain!) is discarded because these values are neither sought nor do they affect the vapor domain values obtained for the well-posed vapor domain problem. The temporary fixing of $\{u_2^i, v_2^i, \theta_2^i\}$ on the interface $\delta(x,t)$ in Fig. 4(*b*) is accomplished by, respectively, adding terms called t_{12}, t_{22}, and t_{32} to the right sides of the *x*-momentum, *y*-momentum, and the energy equations in Eq. (2) with $I=2$. These terms are defined as

$$t_{12} \equiv u_2 * A_1(\mathbf{x}_{\Sigma I}) * \breve{\delta}(|\mathbf{x}-\mathbf{x}_{\Sigma I}|) - u_2^i * A_1(\mathbf{x}_{\Sigma I}) * \breve{\delta}(|\mathbf{x}-\mathbf{x}_{\Sigma I}|)$$

$$t_{22} \equiv v_2 * A_2(\mathbf{x}_{\Sigma I}) * \breve{\delta}(|\mathbf{x}-\mathbf{x}_{\Sigma I}|) - v_2^i * A_2(\mathbf{x}_{\Sigma I}) * \breve{\delta}(|\mathbf{x}-\mathbf{x}_{\Sigma I}|)$$

$$t_{32} \equiv \theta_2 * A_3(\mathbf{x}_{\Sigma I}) * \breve{\delta}(|\mathbf{x}-\mathbf{x}_{\Sigma I}|) - \theta_2^i * A_3(\mathbf{x}_{\Sigma I}) * \breve{\delta}(|\mathbf{x}-\mathbf{x}_{\Sigma I}|). \tag{18}$$

In Eq. (18) above, $\breve{\delta}$ is a "delta function" (see Greenberg [42]) with $\mathbf{x}$ being the vectorial distance of any point from the origin. Also, in Eq. (18), $\mathbf{x}_{\Sigma I}$ is the position vector from the origin to any point on the interface. With the additional terms in Eq. (18) added to the appropriate equations on the right side of Eq. (2), the modified equations are discretized. The resulting equations and their treatment, with appropriate choices of the interfacial-cell constants A_I $(I=1,2,3)$, lead (see Section 3.3 of Liang [2]) to the "source term method" and its results given in Eqs. (7.11)–(7.13) of Patankar [40]. The result of the above modifications is that the original equations in Eq. (2) continue to hold in the interior while the chosen values of $\{u_2^i, v_2^i, \theta_2^i\}$ get fixed on the interface $\delta(x,t)$.

To obtain separate calculations for the liquid domain in Fig. 4*a* and to keep the interface sensitive to the pressure and shear conditions (as given by Eqs. (4)–(5)) at the interface, instead of guessing and temporarily fixing values of $\{u_1^i, v_1^i, \theta_1^i\}$ on the interface $\delta(x,t)$ of Fig. 4(*a*), a scheme (described and termed the "τ-p" method in Yu [17] and Liang [2]) is employed where $\{u_{1s}^i, v_{1s}^i, \theta_1^i\}$ are guessed and fixed on the shifted interface $\delta_{\text{shift}}(x,t)$ of Fig. 4(*b*). This extension of the liquid domain into the vapor domain by a single liquid *interface cell* (as depicted in the inset of Fig. 3 and shown as the gray region in Fig. 4(*a*)) is only for temporary computational convenience of fixing $\{u_{1s}^i, v_{1s}^i, \theta_1^i\}$ on $\delta_{\text{shift}}(x,t)$ by the "source term method." This method is identical to the one described earlier for fixing $\{u_2^i, v_2^i, \theta_2^i\}$ on $\delta(x,t)$ for the vapor domain calculations in Fig. 4(*b*). In this "τ-p" method (see Liang [2]), the values of u_{1s}^i are adjusted to ensure that the appropriate relationship between the tangential stresses, i.e., Eq. (5), is satisfied. Similarly v_{1s}^i values are adjusted to ensure that the appropriate relationship between the normal stresses π_1^i and π_2^i, i.e., Eq. (4), is satisfied. The values of θ_1^i are presented to satisfy Eq. (9). After the satisfaction of the pressure, shear, and temperature conditions on the actual interface $\delta(x,t)$, the entire solution underneath the actual liquid domain $\delta(x,t)$ is retained and the solution for the "ghost" liquid of Fig. 4(*a*) and the solution above $\delta_{\text{shift}}(x,t)$ are discarded. In short this method of fixing and adjusting $\{u_{1s}^i, v_{1s}^i, \theta_1^i\}$ on $\delta_{\text{shift}}(x,t)$ of Fig. 4(*a*) allows one to find and adjust $\{u_1^i, v_1^i, \theta_1^i\}$ on the actual interface $\delta(x,t)$ of Fig. 4(*a*) while concurrently satisfying the pressure (Eq. (4)), shear (Eq. (5)), and temperature (Eq. (9)) conditions on the actual interface.

It is important to note that the liquid and the vapor interface cells depicted in the inset of Fig. 3 are not used to *explicitly* satisfy mass, momentum (normal and tangential), energy, etc. restrictions on this cell. In this sense this approach is unlike some of the *interface capturing* and *interface tracking* approaches where balance laws are *explicitly* invoked for the interface cells. The interface cells (see insets in Fig. 3) are only *indirectly* used here to come up with a computational procedure where the values $\{u_1^i, v_1^i, \theta_1^i, u_2^i, v_2^i, \theta_2^i, \delta\}$ are so adjusted that their converged values satisfy the *discretized* form of all the seven interface conditions—viz. two for temperature (Eq. (9)), two for momentum (Eqs. (4)–(5)), two for mass (Eq. (8)), and one for continuity of tangential velocities (Eq. (3)). Recall that the aforementioned equations that are used were independently and analytically obtained to represent the restrictions imposed by various physical requirements at a sharp interface.

Between times "t" and "$t+\Delta t$," adaptive grids (termed grid A and grid B) are employed. At time *t*, grid A (as in Fig. 3) is based on the geometrical features of $\delta(x,t)$ as a function of *x*, and it changes whenever the liquid and the vapor flow variables need to be recomputed for a changed interfacial configuration $\delta(x,t)$. However, to make the best changes in $\delta(x,t)$ which leads to accurate prediction of δ at time "$t+\Delta t$," a different grid (grid B) is generally required for the variables ($\delta(x,t)$, etc.) appearing in the *interface tracking equation* (which results from one of the interface conditions and has one less spatial dimension as in Eq. (21) below) for this problem. Thus relevant variable values on grid A are mapped onto grid B, and the best predictions for changes in $\delta(x,t)$ are obtained on grid B. These predicted values of $\delta(x,t)$ are then interpolated back to obtain corresponding values on grid A. At any time *t*, linear interpolations are employed for the exchange of relevant flow variable values between grid A and grid B.

Procedural Steps. The final solution is obtained by solving the liquid and vapor domains *separately* and *iteratively* under repeated modifications of the interface configuration $\delta(x,t)$. The iterations modify, intimately connect, and converge the two solutions with the help of all the interface and boundary conditions. This convergence is accomplished through the following substeps:

(***a***) As described earlier, obtain grid A with the help of suitably selected points P_i on an initial guess or a tentative intermediate prediction of the interface location.

(***b***) First extend the liquid domain by a single *interface cell* (depicted in Fig. 3 and shown as the gray region in Fig. 4(*a*)) to define $\delta_{\text{shift}}(x,t)$ as a *shifted extension* of $\delta(x,t)$. Utilizing the "τ-p" method described above and using guessed values of $\{u_{1s}^i, v_{1s}^i, \theta_1^i\}$ on the estimate for shifted interface $\delta_{\text{shift}}(x,t)$ of Fig. 4(*a*), obtain a finite volume solution (SIMPLER technique of Patankar [40]) for the liquid domain underneath $\delta(x,t)$.

If unsteady solutions for $t>0$ are being sought, one skips the remaining operations described here in this paragraph and moves on to the next substep (c). However, for obtaining the steady solution at $t=0$, another liquid domain problem underneath the actual interface $\delta(x,t)$ is solved to *incorporate* the exit-condition prescription necessary for obtaining a *unique* steady solution. For this, the just obtained values of liquid velocity components (u_1^i, v_1^i) and temperature θ_1^i from the "τ-p" method (which involves $\delta_{\text{shift}}(x,t)$) are now temporarily fixed on the actual interface location $\delta(x,t)$. The values of *x*-component of interfacial velocity u_1^i and temperature θ_1^i are retained as they are while the

y-component of interfacial velocity v_1^i is modified to satisfy the current status of the equation $\dot{m}_{LK}=\dot{m}_{\text{Energy}}$. This is in preparation to achieve closure with the subsequent chain of mass flux equalities viz.: $\dot{m}_{VK}=\dot{m}_{\text{Energy}}$ in substep (c) below, and the exit condition restriction imposed as $(\dot{m}_{VK})_{\text{modified}}=\dot{m}_{\text{Energy}}$ in substeps (d)–(e) below.

(*c*) Making use of the vapor domain calculation method described earlier, obtain guesses for $\{u_2^i, v_2^i, \theta_2^i\}$ on the interface $\delta(x,t)$ in Fig. 4(*b*) and then solve the vapor domain flow problem by a finite volume technique (SIMPLER technique of Patankar [40]). Utilizing the liquid domain solution in substep (a) above; values of u_2^i are obtained from a first order discretization of the *continuity of tangential velocities* condition in Eq. (3), values of v_2^i are obtained from a discretization of the requirement $\dot{m}_{VK}=\dot{m}_{\text{Energy}}$ in Eq. (8), and values of θ_2^i are obtained from the thermodynamic restriction in Eq. (9).

(*d*) While obtaining unsteady solutions for $t>0$, this substep is skipped, and one moves on to the next substep (e). However, to obtain a steady solution at $t=0$, it is necessary to prescribe an exit vapor quality Z_e at $x=x_e$. For this, a modified vapor mass flux $(\dot{m}_{VK})_{\text{modified}}\equiv\beta\cdot\dot{m}_{VK}$ is introduced. The parameter β is then explicitly determined so as to make the total vapor mass transfer rate across the entire interface (computed as $\int_0^{x_e}\rho_1/\rho_2\cdot(\dot{m}_{VK})_{\text{modified}}\cdot\sqrt{1+\delta_x^2}\cdot dx$) consistent with the given value of exit quality Z_e (i.e., it is made equal to $1-Z_e$). To account for changing vapor control volume and moving interface, suitable modifications of this approach is needed to specify exit conditions for compressible unsteady cases not considered in this paper. Once β is obtained, the interfacial values of liquid velocity v_1 (denoted as v_1^i) are updated so as to satisfy, for steady flows, the additional exit constraint:

$$\dot{m}_{LK}=(\dot{m}_{VK})_{\text{modified}}. \tag{19}$$

The steady solution procedure then moves to the next substep (e) to update $\delta(x)$ values from Eq. (22) given below at the end of substep (e).

(e). The only remaining interface condition $\dot{m}_{LK}=\dot{m}_{\text{Energy}}$ in Eq. (8) (which, for steady flow computations, because of Eq. (19) above, becomes $(\dot{m}_{VK})_{\text{modified}}=\dot{m}_{\text{Energy}}$) is satisfied in this substep. It should be noted that the physical variable form $\dot{m}_{LK}=\dot{m}_{\text{Energy}}$ of this equation arises from Eq. (*A*7) in the Appendix, and can be written in the following popular form for *tracking* the interface $\mathcal{H}(x,y,t)=0$:

$$\frac{\partial\mathcal{H}}{\partial t}+\mathbf{v}_1^i\cdot\nabla\mathcal{H}\cong\left.\frac{-k_1}{\rho_1\cdot h_{fg}}\frac{\partial\mathcal{T}_1}{\partial n}\right|^i\cdot|\nabla\mathcal{H}|. \tag{20}$$

Focusing on locating the interface prior to any break up or pinch off, the interface $\mathcal{H}$ in Eq. (20) is represented by a simple single valued form given by $\mathcal{H}=y-\Delta(x,t)=0$. Nondimensionalizing the resulting Eq. (20) under Eq. (1), the following nonlinear and hyperbolic interface tracking equation is obtained:

$$\frac{\partial\delta}{\partial t}+\overline{u}(x,t)\frac{\partial\delta}{\partial x}=\overline{v}(x,t), \tag{21}$$

where $\overline{u}\equiv u_1^i+\{\text{Ja}/(\text{Re}_1\cdot\text{Pr}_1)\}\partial\theta_1/\partial x|^i$ and $\overline{v}\equiv v_1^i+\{\text{Ja}/(\text{Re}_1\cdot\text{Pr}_1)\}\partial\theta_1/\partial y|^i$ typically depend strongly, but indirectly, on δ. While obtaining the steady solution at $t=0$, however, all time derivatives are set equal to zero, and the interface is updated by a simple numerical integration (trapezoid rule) of the *steady form* of Eq. (21), which is

$$d\delta/dx=\overline{v}(x)/\overline{u}(x)\quad\text{for}\quad x>0. \tag{22}$$

In this substep, Eq. (21) or Eq. (22) is solved to obtain new values of δ. For the steady case, Eq. (22) yields new $\delta_{\text{steady}}(x)$ and for the unsteady case, Eq. (21) is solved to obtain new values of δ for the next time step "$t+\Delta t$" or is used merely to improve the existing estimates of δ and other flow variables for time "$t+\Delta t$." Whatever be the case, at each relevant x, all liquid and vapor flow variables are linearly mapped to the new liquid and vapor domains defined by each new prediction of the interface location.

Repetition of the steps (a)–(e) above with a starting guess $\delta_{\text{guess}}(x)$ for the interface location leads first to a convergent solution $\delta_{\text{steady}}(x)$ of the steady equations. This solution is consistent with the prescribed exit quality Z_e because β introduced and computed in substep (d) above satisfies the requirement of $\beta\to1$. Starting from this converged steady solution at $t=0$, steps (a)–(e) above are repeated a suitable number of times for each new time step, viz. $t=\Delta t$, $t=2\Delta t$, etc. This leads to a convergent unsteady solution consistent with the choice of initial and boundary data. The ability to improve the results at any time step by dwelling at that time step for repeated iterations between the time step under consideration and the previous time step makes the process of forward time marching *implicit* (or, more appropriately, *semi-explicit*).

The solution obtained by the above procedure not only satisfies the pressure, shear, temperature, and continuity of tangential velocity conditions at the interface, but also satisfies the various flow field restrictions that arise from having a nonzero interfacial mass flux $\dot{m}$. The *steady solutions* at $t=0$ satisfy $\dot{m}_{LK}=\dot{m}_{\text{Energy}}$ in substep (a), $\dot{m}_{VK}=\dot{m}_{\text{Energy}}$ in substep (b), and the exit condition restriction imposed as $(\dot{m}_{VK})_{\text{modified}}=\dot{m}_{\text{Energy}}$ in substeps (d)–(e). The *unsteady solutions* at $t>0$ satisfy $\dot{m}_{VK}=\dot{m}_{\text{Energy}}$ in substep (b) and $\dot{m}_{LK}=\dot{m}_{\text{Energy}}$ in substep (d).

Discussions for the Interface Tracking Equation and Its Solution. When the right side of Eq. (20) is zero, spatial extension of Eq. (20) leads to a color function $\mathcal{H}$ whose initial values $\mathcal{H}=0$ and $\mathcal{H}=1$ within each of the phases are retained for all times $t>0$, and this forms the basis of the popular VOF (volume of fluids) techniques (see Hirt and Nicholas [24], etc.) for air/water type flows. Similarly, a suitable spatial extension of Eq. (20), in conjunction with some other techniques, is used in the level-set method (Sussman et al. [22], etc.) for *capturing* the interface through iterative single domain (consisting of both the phases) calculations. For boiling related phase change flows, the level-set technique has recently been used by Son and Dhir [23]. In order to better understand and sidetrack some of the problems (see, e.g., Li and Renardy [27]) associated with interface *capturing* techniques (be it level-set, VOF, etc.) that utilize Eq. (20), we look at the existing knowledge base for the reduced form of Eq. (20) given in Eq. (21). Equation (21) is the *interface tracking equation* which, for $t>0$, defines the following *interface tracking problem:*

$$\frac{\partial\delta}{\partial t}+\overline{u}(x,t)\frac{\partial\delta}{\partial x}=\overline{v}(x,t)$$

$$\delta(0,t)=0$$

$$\delta(x,0)=\delta_{\text{steady}}(x)\quad or\quad\text{other prescriptions}. \tag{23}$$

The computational issues for discretization and numerical solution of Eq. (23) are well understood and extensively discussed in Abbott and Basco [26] with regard to various algorithms' stability and accuracy in determining both the amplitude and the phase of its often-wavy numerical solutions. It is known from there that among various possible discretizations for Eq. (23), the one that gives best results in marching from (x,t) to $(x+\Delta x,t+\Delta t)$ has a Courant number Cr ($\text{Cr}\equiv\overline{u}(x,t)\cdot\Delta t/\Delta x$) equal to 1 (i.e., $\text{Cr}\cong1$) and the following discretizations:

$$\delta(x+\Delta x,t+\Delta t)=\delta(x,t)+\overline{v}(x,\tau)\cdot\Delta t$$

$$\partial\delta/\partial t=[\,\delta(x+\Delta x,t+\Delta t)-\delta(x+\Delta x,t)]/\Delta t$$

$$\partial\delta/\partial x=[\,\delta(x+\Delta x,t)-\delta(x,t)]/\Delta x. \tag{24}$$

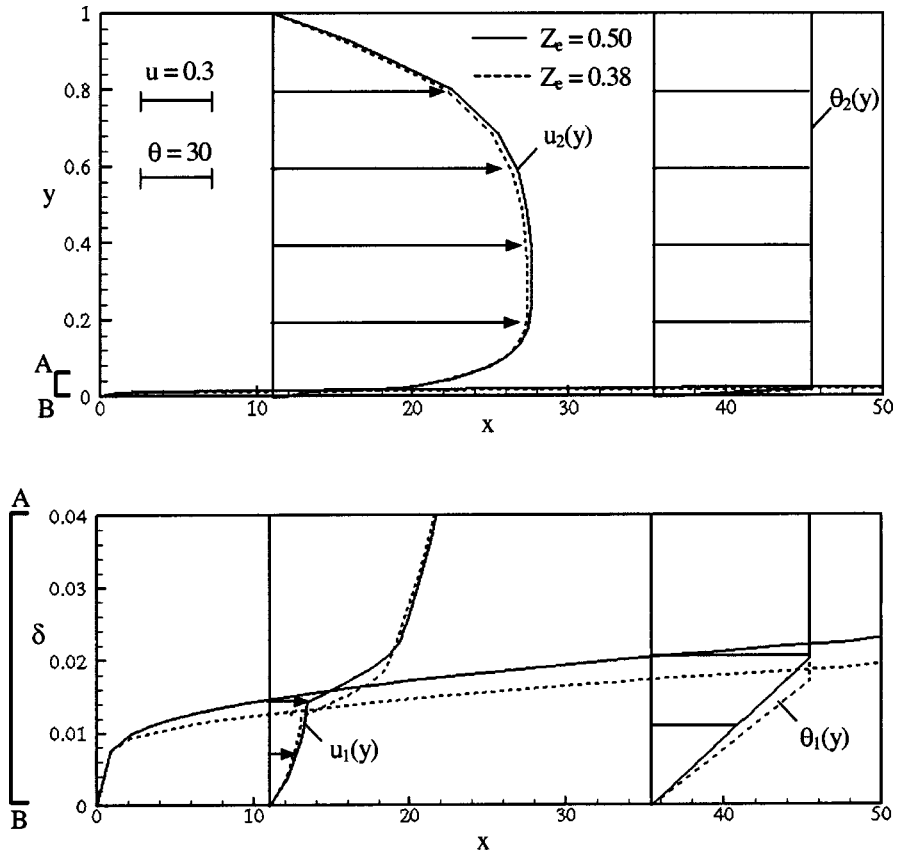

Fig. 5 The above predictions are for vertical channel flows of saturated R-113 vapor. The flow cases are specified in Table 1 with $\alpha=90$ deg, $x_e=50$ and two different exit conditions, viz. $Z_{e_1}=0.5$ and $Z_{e_2}=0.38$.

The intermediate time $\tau\,(t\leqslant\tau\leqslant t+\Delta t)$ in Eq. (24) above (appearing in the definition of Cr through $\overline{u}$ and in the first equation through $\overline{v}$) is chosen such that, by the end of iterations for this time interval, $\overline{u}$ and $\overline{v}$ satisfy $\overline{u}(x,\tau)=\{\overline{u}(x,t)+\overline{u}(x,t+\Delta t)\}/2$ and $\overline{v}(x,\tau)=\{\overline{v}(x,t)+\overline{v}(x,t+\Delta t)\}/2$. It should be noted that one can tentatively use any convenient and stable discretization for $\partial\delta/\partial x$ and $\partial\delta/\partial t$ in substeps (a)–(d) above, as long as the optimal discretizations in Eq. (24) are employed and satisfied *by the end* of repeated iterations of substeps (a)–(e) for any given time step.

The above requirement of $\mathrm{Cr}\equiv\overline{u}\Delta t/\Delta x\approx 1$ in Eq. (24) is handled by mapping the $xu(i)$ locations in grid A to $xud(i)$ locations in grid B (see Fig. 3). This is accomplished by setting, at any time t, $xud(3)=xu(3)=\varepsilon>0$ and sequentially finding all subsequent $xud(i)$ for $i\geqslant 4$ by the relation: $xud(i+1)=xud(i)+\overline{u}(xud(i),t)\cdot\Delta t$ where $\overline{u}(xud(i),t)$ values are also sequentially obtained from linear interpolations within the known set of values of $\overline{u}$ at $xu(i)$ locations. The δ values thus obtained from Eqs. (23)–(24) on grid B are then mapped back to grid A with the help of linear interpolations.

It is further noted that the discretizations in Eq. (24) are the same as the discretizations for the *method of characteristics* (see, e.g., Greenberg [42]). That is, evolution of $\delta(x,t)$ as a solution of Eq. (21) takes place along *characteristic curves* $x=x_c(t)$ given by

$$\frac{dx_c}{dt}=\overline{u}(x_c(t),t)$$

$$x_c(0)=x^* \quad \text{or} \quad x_c(t^*)=0, \tag{25}$$

where x^* is any given value of x between the inlet and the outlet

Table 1 Specification of reported flow situations involving saturated R-113 vapor of the inlet. Properties of R-113 are taken from ASHRAE Handbook, [45].

Fig. # for flow	p_o (kPa)	$\mathcal{T}_s(p_o)$ (°C)	$\Delta\mathcal{T}$ (°C)	h (m)	U (m/s)			
	$\mathrm{Re_{in}}$	Ja	$\mathrm{Fr^{-1}}_x$	$\mathrm{Fr^{-1}}_y$	ρ_2/ρ_1	μ_2/μ_1	We	$\mathrm{Pr_1}$
5, 6, 7, 8a, 8b, 10, 11a, 11b, 11c, 12, 13a, 13b, 14a, 14b, 15, 16, 17, 18	108.855	49.47	5	0.004	0.41			
	1200	0.0341	0.2379	0.32×10^{-6}	0.0053	0.0209	67.6335	7.2236

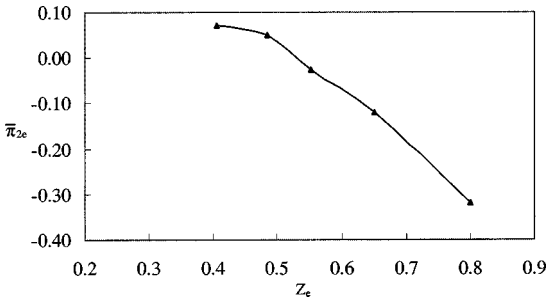

Fig. 6 For the flow situations specified in Table 1 with α=90 deg, x_e=50, the figure shows the equivalence of specifying exit vapor quality Z_e or exit pressure $\bar{\pi}_e \equiv 1/(1-\delta)\int_\delta^1 \pi_2 dy$ to specify exit conditions. It is computationally more convenient to specify exit condition Z_e.

in Fig. 1 and $t^*>0$. Equations (23) and (25) together imply that the evolution of $\delta(x,t)$ along the *characteristic curves* is governed by

$$\frac{d\hat{\delta}(t)}{dt} = \hat{\bar{v}}(t)$$

$$\hat{\delta}(0) = \delta_{\text{steady}}(x^*) \quad or \quad \text{other prescriptions}, \tag{26}$$

where $\hat{\delta}(t) \equiv \delta(x_c(t),t)$ and $\hat{\bar{v}}(t) \equiv \overline{v}(x_c(t),t)$.

It is found that the integrable singularity at $x \sim 0$ is such that replacement of the condition $\delta(0,t)=0$ in Eq. (23) by a condition of the type $\delta(\varepsilon_1,t)=\varepsilon_2$ for any suitably chosen $\varepsilon_1>0$ and $\varepsilon_2>0$ does not affect the solutions at $x \gg \varepsilon_1$. Therefore, unless one is interested in the singularity at $x=0$, the proposed approach works rather well for all cells except the first two to three cells at the leading edge corner (i.e., left corner of Fig. 2). This is because solution obtained away from the leading edge remains largely unaffected by changes in specific reasonable choices made for ε_1 and ε_2. Thus, as expected, integrability of this singularity in two or three-dimensional calculations poses no problem. However, resolution of the same singularity becomes more challenging for one-dimensional approaches (see Narain et al. [19]) that employ semi-empirical interfacial shear models.

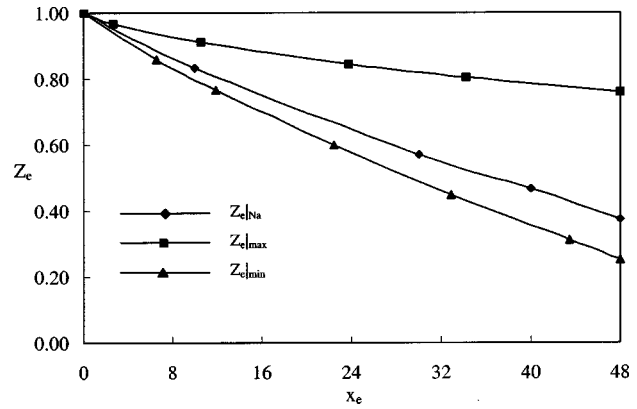

Fig. 7 With all remaining flow parameters specified as in Table 1 with α=90 deg, the above figure shows that exit condition specified by the number Z_e at a given x_e must lie within two well-defined values, viz. $Z_e|_{min}(x_e) \leq Z_e \leq Z_e|_{max}(x_e)$. This restriction, presumably, arises from the fact (see Carey [37]) that the assumed annular/stratified flows only occur within certain parameter ranges.

4 Stability of Steady Solutions and the Role of Exit Conditions

For slow laminar/laminar internal condensing flows considered here, it is computationally shown in Fig. 5 that, for different exit conditions (i.e., exit vapor quality $Z_e = Z_e(0)$), one obtains different steady solutions for any given inlet pressure and inlet mass flow rate. In Fig. 6, we see that the prescription of a different exit vapor quality Z_e is equivalent to a prescription of a different exit pressure $\bar{\pi}_{2e} \equiv 1/(1-\delta)\int_\delta^1 \pi_2 dy$. Because of the nonuniqueness of *steady* solutions in the absence of prescribed exit conditions, the following questions arise with regard to different solutions associated with different Z_e values: (i) all else remaining the same, is there a range of Z_e values that can be prescribed at a given $x=x_e$ for which a range of steady solutions can be obtained; (ii) is a particular steady solution for a given Z_e stable or unstable in the *absence* of exit constraints for $t>0$ (i.e., if $Z_e(0)=Z_e$ but $Z_e(t)$ can take any value for $t>0$); and (iii) is a particular steady solution for a given Z_e stable or unstable in the *presence* of exit constraints for $t>0$ (e.g., $Z_e(t)=Z_e$ for $t \geq 0$)?

Representative answer to question (i) above is given in Fig. 7 which computationally demarcates a range of $Z_e(0)=Z_e$ values for each x_e while all other nondimensional parameters determining the flow are held fixed. The demarcation in Fig. 7 is of the type $Z_e|_{\min} \leq Z_e \leq Z_e|_{\max}$ where the lower and upper bounds are rather well defined. The parameter range shown in Fig. 7 changes as the remaining significant parameters (viz. Re_{in}, Ja, α, ρ_2/ρ_1, μ_2/μ_1, and Pr_1) are changed.

Answer to question (ii) regarding stability of solutions for the unconstrained exit case follows from results given in Figs. 8–9. Based on two-dimensional *unsteady* simulations results shown in Fig. 8(*a*) for the idealized noise-free case and its noise-sensitive quasi-steady counterpart in Fig. 8(*b*), it is found that, for unconstrained exit conditions, as $t \to \infty$, there is an *attractive* solution (see Fig. 9) while the remaining steady solutions are *unstable*. All else being given, the final Z_e value obtained for the attractive solution in Fig. 8(*a*), is denoted as $Z_e|_{\text{Na}}$ to indicate that it is *the* naturally selected value of Z_e in the absence of exit constraints. This naturally selected attractive steady solution for unconstrained exit conditions is found to be *stable* (see definition of *stability* in Joseph [43]) because *initial* two-dimensional disturbances damp out over time. It should be noted that a solution might be *stable* and yet be difficult to realize in practice because of *sensitivity* to certain minuscule noises that are commonly present. To understand the stability and noise sensitivity issues, the problem in Eq. (23) and its solution along characteristics, as defined by Eqs. (25)–(26), is best rewritten in terms of the evolution of a disturbance $\delta'(x,t) \equiv \delta(x,t) - \delta_{\text{steady}}(x)$. Under this change of variables, the characteristics continue to be defined by Eq. (25) while Eq. (23) changes to

$$\frac{\partial \delta'}{\partial t} + \overline{u}(x,t)\frac{\partial \delta'}{\partial x} = \bar{\bar{v}}(x,t)$$

$$\delta'(0,t) = 0$$

$$\delta'(x,0) \quad or \quad \text{other prescriptions}, \tag{27}$$

where $\bar{\bar{v}}(x,t) \equiv [\overline{v}(x,t) - \overline{v}_{\text{steady}}(x) - \{\overline{u} - \overline{u}_{\text{steady}}\}(d\delta_{\text{steady}}/dx)]$ and Eq. (26) changes to

$$\frac{d\hat{\delta}'(t)}{dt} = \hat{\bar{\bar{v}}}(t)$$

$$\hat{\delta}'(0) = 0 \quad or \quad \text{other prescriptions}, \tag{28}$$

where $\hat{\delta}'(t) \equiv \delta'(x_c(t),t)$ and $\hat{\bar{\bar{v}}}(t) \equiv \bar{\bar{v}}(x_c(t),t)$. It should be noted that $|\overline{u} - \overline{u}_{\text{steady}}|$ and $|\bar{\bar{v}}(x,t)|$ are identically zero for steady solutions with $\delta'=0$ and are small for disturbances with small δ'. The attractive solution in Figs. 8–9 is such that disturbances $\delta'(x,t)$ again propagate along characteristics curves given by Eq.

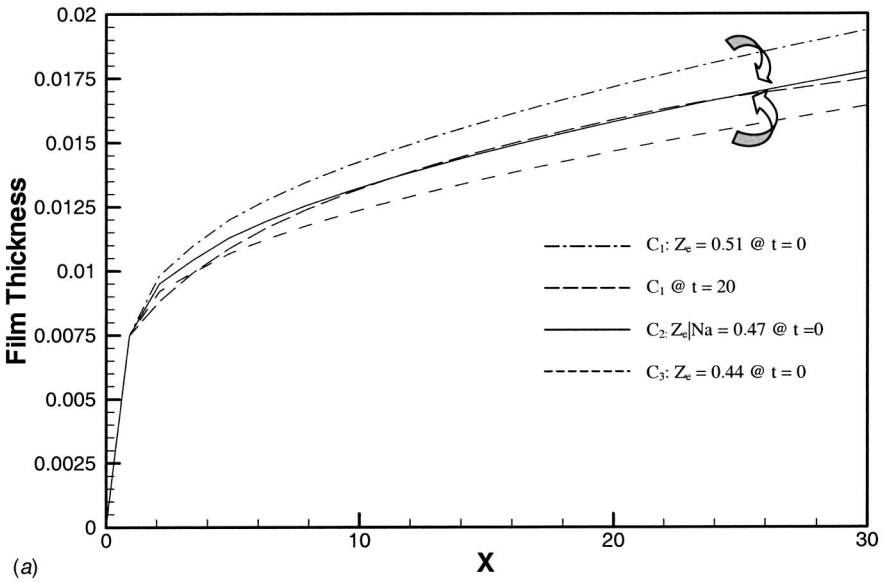

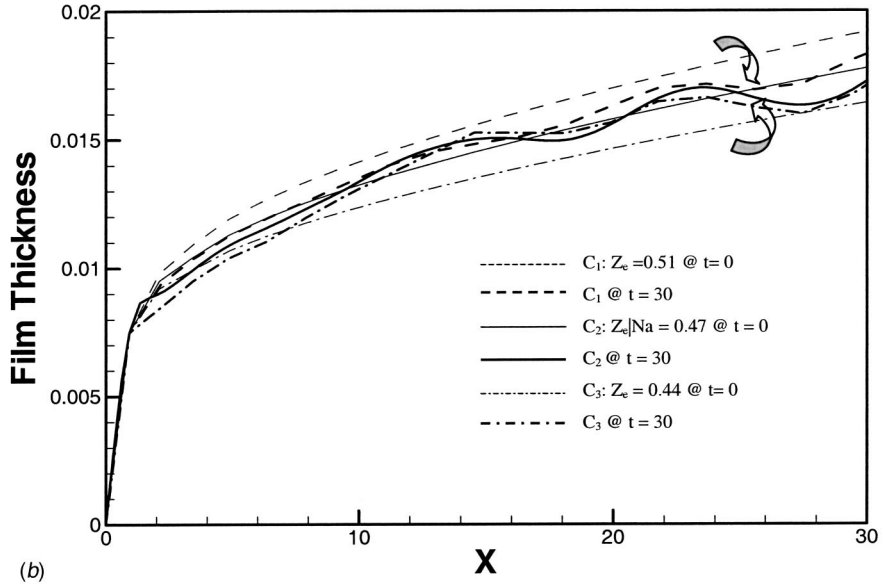

Fig. 8 (*a*) For flow situation specified in Table 1 with α=90 deg and x_e=30, the figure depicts two sets of $\delta(x,t)$ predictions for $t>0$. One curve *C*1 starts at Z_e=0.51 at t=0, and tends, as $t\to\infty$, to the solution for $Z_e|_{Na}$=0.47. The other curve *C*2 starts at Z_e=0.44 at t=0 and tends, as $t\to\infty$, to the same steady $Z_e|_{Na}$ solution. (*b*) For flow situations considered in Fig. 7(*a*), the above predictions for $t>0$ starts at t=0 from the same curves *C*1 and *C*2 in Fig. 7(*a*). However, at $t>0$, there is a condensing surface noise given by $v_1(x,0,t)=\varepsilon\cdot\sin(2\pi x/\lambda)\cdot\sin(2\pi t/T)$, with ε=0.3E-6, λ=10, and T=24. As $t\to\infty$, the mean part of wavy quasi-steady solutions coincides with the smooth solution, shown in Fig. 8(*a*) for $Z_e=Z_e|_{Na}$=0.47.

(25). For the steady solution in Fig. 10, representative characteristics curves C_1, C_2, etc. are shown in Fig. 11(*a*). These curves are generated by numerical integration (fourth-order Runge Kutta) of Eq. (25) with the characteristic speed $\overline{u}(x,t)=\overline{u}_{\text{steady}}(x)$. Figure 11(*b*) shows that the characteristics speed for small initial disturbances (which, because of the nature and form of Eq. (27), is the same as phase speed) satisfies $\overline{u}(x,t)\cong\overline{u}_{\text{steady}}(x)$. For *intrinsic* waves induced by small initial disturbances, unlike gravity waves on water (see Lighthill [31]), the waves are nondispersive (i.e., wave speeds are nearly independent of wavelengths) and become somewhat dispersive only for large amplitude initial disturbances (see $\overline{u}$ for this case in Fig. 11(*b*)). For the steady and initial dis-

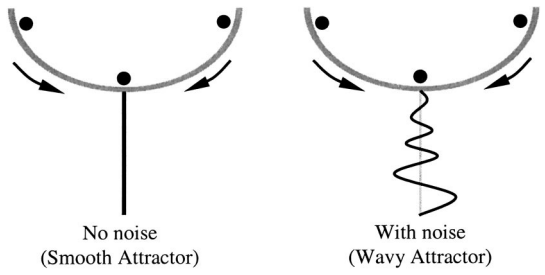

Fig. 9 Qualitative nature of the stable, steady/quasi-steady solutions

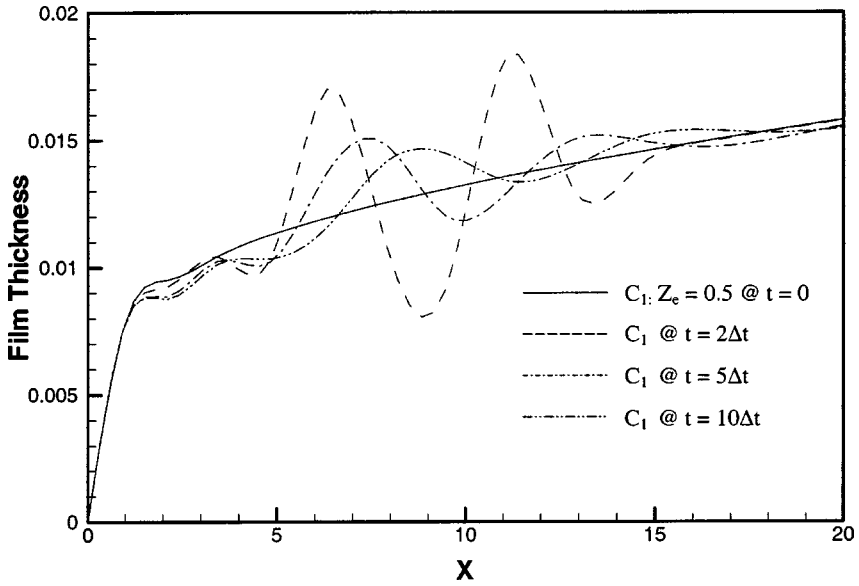

Fig. 10 For flow situations specified in Table 1 with α=90 deg and x_e=20, the above $\delta(x,t)$ predictions (Δt=2.5) are for initial data $\delta(x,0)=\delta_{steady}(x)+\delta'(x,0)$, where a nonzero disturbance $\delta'(x,0)$ has been superposed at t=0 on the steady solution δ_{steady} (shown as curve $C1$ above for $t<0$). The steady solution corresponds to $Z_e=Z_e|_{Na}$=0.5. Here $\delta'(x,0)=0$ except in the interval $x^*<x<x^*+10$, where x^*=3.5 and $\delta'(x,0)=0.5\cdot\delta_{steady}(x)\cdot\sin(2\pi x/5)$. It is clear that even this *large* a disturbance damps at later times.

turbance cases shown in Fig. 10, Fig. 11(c) shows values of the "growth/damping" factor $\hat{\bar{v}}(t)$ along a representative characteristic curve (such as C_1 in Fig. 11(a)). The initial disturbance in Fig. 10 typically damps because, in Fig. 11(c), we have a typical response of $\hat{\bar{v}}(t)<0$ for all sufficiently large t and $\delta'(x_c(t),t)=\delta'(x^*,0)+\int_0^t\hat{\bar{v}}(\tau)\cdot d\tau$ tends to zero as $t\to\infty$ along characteristics originating on the $t=0$ line. Furthermore, besides damping of initial disturbances along the characteristics curves, disturbances leave the computational domain ($0\leqslant x\leqslant x_e$) with a forward phase speed of $\overline{u}>0$. As a result, in Fig. 11(a)), at a fixed x as $t\to\infty$, one would leave the solid line initial disturbance characteristics originating on the $t=0$ line and get on the characteristics originating on the $x=0$ line (these curves are over $t\geqslant t^*$ for any $t^*>0$). The values of δ' on these characteristics (over $t\geqslant t^*$ and $t^*>0$) are not affected by the nonzero initial disturbances since these characteristics only carry the nearly zero-noise information of $\delta'(0,t)\approx 0$ for all $t\geqslant t^*$. This stability of a natural steady solution associated with the exit condition $Z_e=Z_e|_{Na}$ is typically true for any initial disturbance (not just the large initial disturbance example used in Fig. 10) under unconstrained exit conditions. While the small intrinsic initial disturbance waves damp out as they propagate downstream with increasing wavelengths and increasing speed $\overline{u}\approx\overline{u}_{steady}(x)$. For the initial disturbance cases with initial wavelength λ, at later times t the wavelengths $\bar{\lambda}(x,t)=\bar{\lambda}(x_c(t),t)$ with $\bar{\lambda}(x_c(0),0)=\lambda$. Here reciprocal of $\bar{\lambda}(x,t)$, as in Lighthill [33], is in terms of x-derivative of phase angles that are constant as they propagate along the characteristics curves. Since these derivatives get smaller with increasing x because of the increasing x-separation among incrementally apart characteristics (this is also the case with finitely spaced characteristics C_1, C_2, etc. shown in Fig. 11(a) the wavelengths $\bar{\lambda}(x,t)$ increase as the disturbances propagate forward under continued damping.

Earlier, in Fig. 5, it was shown that different steady solutions are possible for different exit constraints (i.e., different values of Z_e). With regard to stability of such steady solutions to initial disturbances while *exit conditions* are constrained to keep values of Z_e fixed in the *immediate vicinity* of $Z_e|_{Na}$, stability, like the $Z_e=Z_e|_{Na}$ solutions, are expected. However, unsteady simulations for initial disturbances while retaining exit constraint at all times are outside the scope of this paper as such simulations require allowance of density fluctuations in the vapor phase and accounting for their interactions with fluctuations in other variables. It is, however, easily conjectured that many steady solutions with constrained the values (at all times) *sufficiently far* from $Z_e|_{Na}$, such as $Z_e=0.26$ case shown in Fig. 12 (with its unlikely liquid velocity profiles resulting from the inappropriate constant density assumptions), will have oscillatory *instability* in response to initial disturbances. This is because sustained density and other fluctuations/waves are expected.

5 Effects of Noise and Resonance Condition

The *natural* and *stable* solutions described in Fig. 9 and obtained in Fig. 8 were shown, in Fig. 10, to be *intrinsically wavy* to initial disturbances. It is shown in Fig. 13(a) that, despite the *stability*, the interface is quite sensitive to even minuscule vibrations of the bottom plate. This is because transverse condensate velocity component v_1 is very small (e.g., if axial vapor velocity is $O(1)$, axial condensate velocity is often about $O(10^{-3})$, and transverse condensate velocity is often about $O(10^{-5})$) and yet it is a significant player in the forcing term on the right side of the interface tracking equation in Eq. (23). The small bottom plate noises considered in this paper correspond to a velocity $v_1(x,0,t)=\varepsilon\cdot\sin(2\pi x/\lambda)\cdot\sin(2\pi t/T)$ whose amplitude ε is in the range of $1\times10^{-5}-3\times10^{-5}$. For the representative cases considered here (e.g., $T=12$, $\lambda=5$, $h=.004$ m, and $U=0.41$ m/s), the maximum displacement amplitude of the vibrations is about 0.25 μm, the maximum velocity amplitude is about 0.12 μm/s, and the maximum acceleration amplitude is about 6.25×10^{-4} m/s^2 (which is less than 10^{-4} g, g$\cong$10 m/s^2). Such transverse condensing surface vibrations are typically induced by structural or coolant noise sources and are indeed commonly present in the 0–30 Hz range considered here. Thus these noise-induced waves

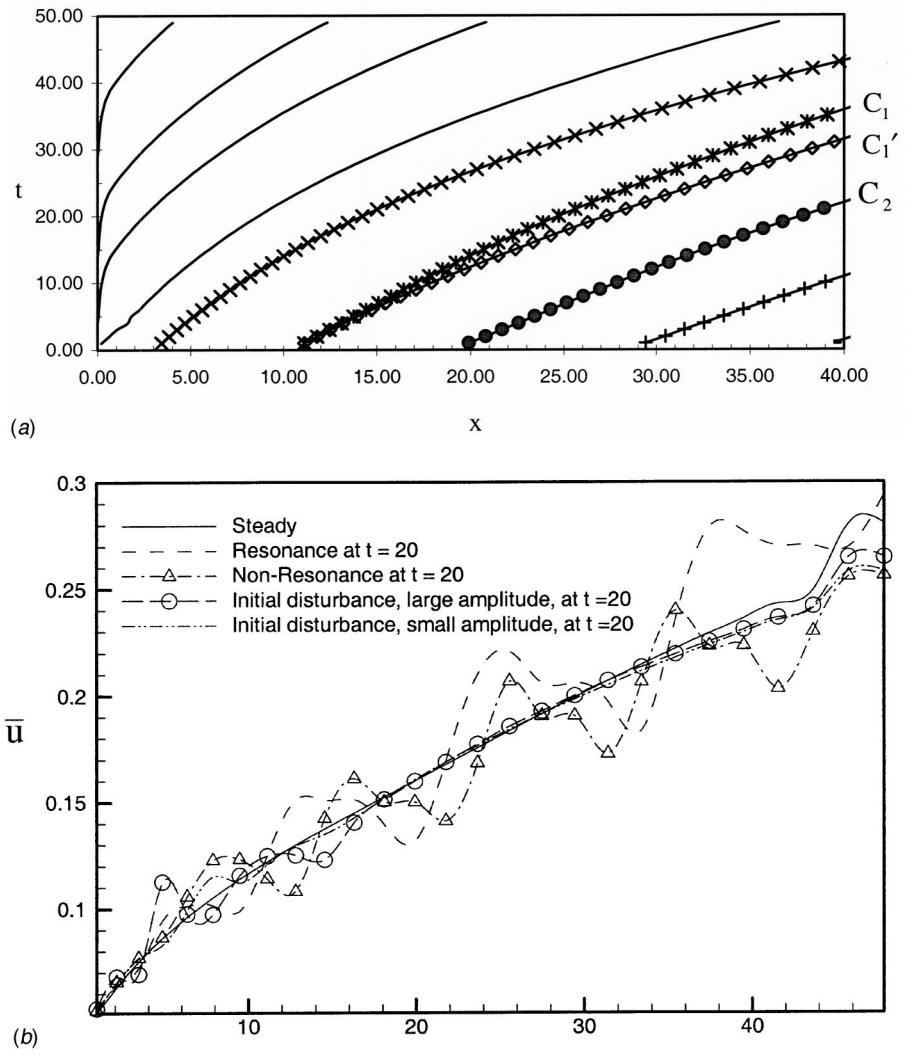

Fig. 11 (*a*) **For flow situation specified in Table 1 with α=90 deg and x_e=40, the characteristics curve C_1 denote curves along which infinitesimal initial disturbances naturally propagate on the stable steady solution. Curve C_1' denotes characteristics along which finite disturbance arising from forced bottom wall noise actually propagate. On characteristics originating at x=0, $\delta(0,t)\cong 0$ implies $\delta'\cong 0$.** (*b*) **For flow situations defined in Table 1 with α=90 deg and x_e=48, the above $\bar{u}(x,t)$ predictions for $t\geqslant 0$ are for** (i) **steady flow with $Z_e|_{Na}$=0.524,** (ii) **resonant case in Fig. 13,** (iii) **nonresonant case in Fig. 13,** (iv) **large initial disturbance of Fig. 10 and** (v) **small initial disturbance $\delta'(x,0)$ which is one-fifth of $\delta'(x,0)$ in Fig. 10.** (*c*) **For flow situations defined in Table 1 with α=90 deg and x_e=50, the above $\bar{\bar{v}}(t)$ values are along actual characteristics curves like C_1' in Fig. 11(*a*). The predictions are for** (*i*) **the steady and stable flow with $Z_e|_{Na}$=0.578,** (*ii*) **the resonant case of Fig. 13,** (*iii*) **the nonresonant case of Fig. 13, and** (iv) **the small initial disturbance case** (**scaled up and shown in the lower figure**) **in Fig. 11(*c*).**

discussed/studied here are the waves that appear as wavy interfacial oscillations in laminar/laminar condensing flows under unconstrained exit conditions.

The Fourier component of the standing-wave disturbance $v_1(x,0,t)$ used in Fig. 13(*a*) is equivalently written as the sum of two traveling waves. Denoting the forward traveling wave's phase angle as $\alpha_1 \equiv 2\pi\{x/\lambda - t/T\}$ and the backward traveling wave's phase angle as $\alpha_2 \equiv 2\pi\{x/\lambda + t/T\}$, the bottom plate noise is given as

$$v_1(x,0,t) = \frac{\varepsilon}{2}[\mathrm{Re}\{\exp(i\alpha_1(x,t)) - \exp(i\alpha_2(x,t))\}], \quad (29)$$

where "i" in the arguments of the exponential functions appearing in Eq. (29) denotes the complex number $\sqrt{-1}$ and "Re{ }" in Eq. (29) denotes real part of the expression within "{ }."

Furthermore, results in Figs. 13(*a*) are in accord with the expectation (see Miyara [32] for the Nusselt problem) that noise amplification is either sustained or increased with increasing downstream distances and film thickness values. For resonant or nonresonant condensing surface vibration considered in Fig. 13, the corresponding oscillatory "growth/damping" factor $\bar{\bar{v}}(t)$ values in Fig. 11(*c*) (computed along the actual unsteady characteristics such as C_1' of Fig. 11(*a*)) are also, on average, either sustained or amplified. In Fig. 11(*b*), at large times, the noise-induced

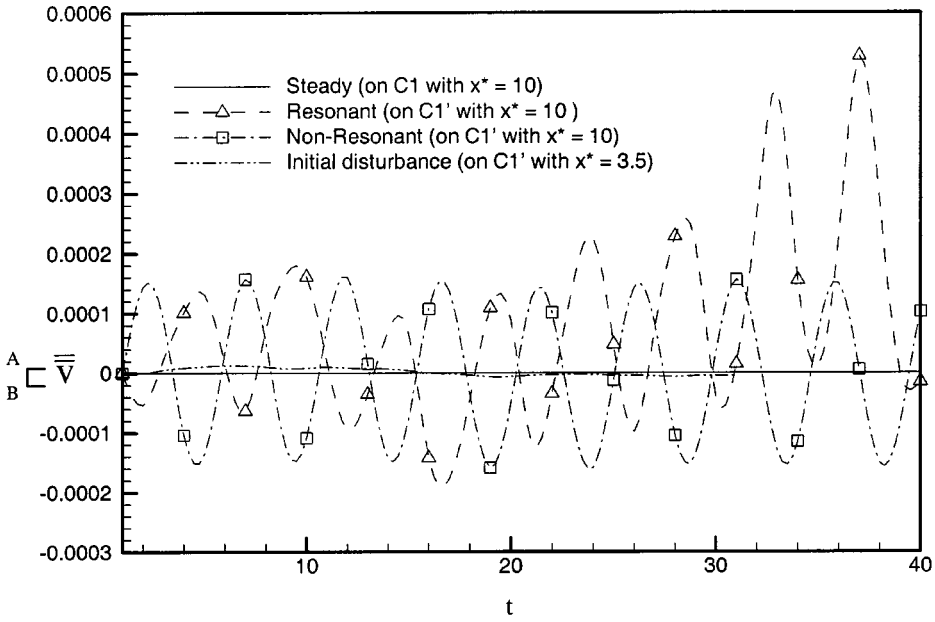

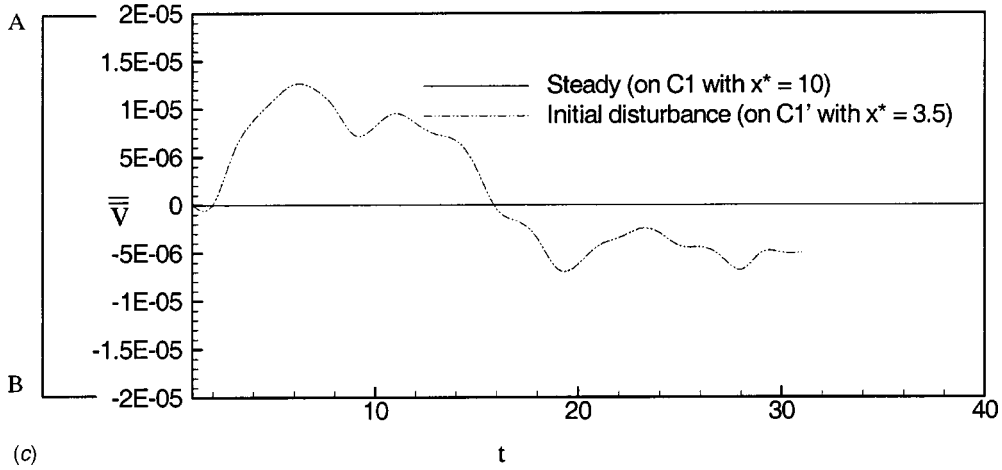

(*c*)

Fig. 11 (***continued***)

waves' characteristics speed $\overline{u}(x,t)$ has a mean $\overline{u}_{\text{mean}}(x)$ (with $\overline{u}_{\text{mean}}(x) \cong \overline{u}_{\text{steady}}(x)$) and superposed oscillations/waves on $\overline{u}_{\text{mean}}(x)$. It is seen in Fig. 11(*a*) that the *integration* involved in obtaining the characteristics C_1', C_2', etc. smooth out the effects of the fluctuating part of $\overline{u}(x,t)$ while its mean $\overline{u}_{\text{mean}}(x)$ mainly affects the *characteristics* at large *x*-locations where the noise effects are large and nonlinear effects associated with the size of $|\delta'(x,t)|$ play a role. For the nonresonant wall noise case in Fig. 13(*a*), both the "growth/damping" factor $\bar{v}(x,t)$ values (shown in Fig. 11(*c*) as $\hat{\bar{v}}(t)$ along C_1) and $\delta'(x,t)$ values have been computationally verified to sustain waves with approximately the same wavelength λ and frequency $f_{\text{ext}} = 1/T$ as that of the external forcing noise. Thus the phase angles associated with these interfacial waves are same as those associated with the forcing noise in Eq. (29). To better understand the connection between these two variables in terms of the resulting phase speeds and the intrinsic phase speed for the flow, analytical implications of Eq. (23) are presented next for the case of small amplitude bottom wall noise.

For the purpose of identification of resonance conditions, it is assumed, as is the case in Fig. 11(*b*), that an amplitude "ε" for bottom wall noise can be found up to which (i.e., small to moderate values of ε) the approximation $\overline{u}(x,t) \cong \overline{u}_{\text{steady}}(x)$ holds. The above discussions for the bottom plate noise in Eq. (29) allow us to assume that the form of $\bar{v}(x,t)$ and the form of the associated $\delta'(x,t)$ are given by

$$\bar{v}(x,t) = \text{Re}\{v_{g1}(x,t)\exp(i\alpha_1(x,t) + v_{g2}(x,t)\exp(i\alpha_2(x,t)\}$$

$$\delta'(x,t) = \text{Re}\{\varsigma_{g1}(x,t)\exp(i\alpha_1(x,t) + \varsigma_{g2}(x,t)\exp(i\alpha_2(x,t)\}, \tag{30}$$

where the phase angles α_1 and α_2 are same as in Eq. (29). Furthermore *complex-valued* growth rates v_{g1} and v_{g2} for $\bar{v}(x,t)$ and ς_{g1} and ς_{g2} for $\delta'(x,t)$ are assumed to be non-oscillatory. Under this assumption of nonoscillatory $\overline{u}(x,t) \cong \overline{u}_{\text{mean}}(x)$, the relationships among the growth rates for $\bar{v}(x,t)$ and $\delta'(x,t)$ are found by substituting Eq. (30) in Eq. (27) and equating coefficients of the two exponentials. This gives

$$\frac{d\varsigma_{g1}}{dt} + i(D\Delta_1)\varsigma_{g1} = v_{g1}$$

$$\frac{d\varsigma_{g2}}{dt} + i(D\Delta_2)\varsigma_{g2} = v_{g2}, \tag{31}$$

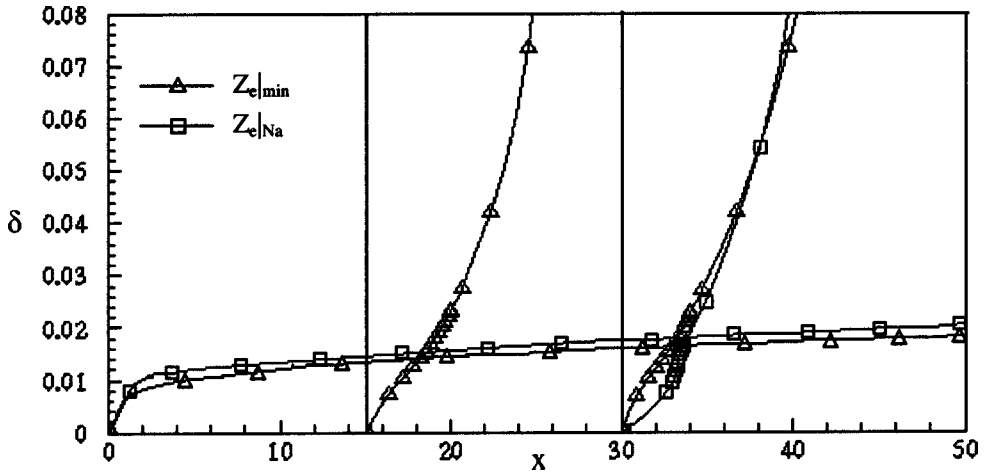

Fig. 12 For the above flow situation specified in Table 1 with α=90 deg and x_e=50, the steady solutions are obtained for $Z_e=Z_e|_{min}=0.26$ and $Z_e|_{Na}=0.36$

where $D\Delta_1 \equiv (2\pi\overline{u}/\lambda - f_{ext})$, $D\Delta_2 \equiv (2\pi\overline{u}/\lambda + f_{ext})$, $f_{ext} \equiv 1/T$, and the *ordinary* time derivatives in Eq. (31) are taken along the characteristics $x = x_c(t)$ defined in Eq. (25). With $J=1$ or 2 denoting the numerical subscripts in Eq. (31), the solutions of the two equations in Eq. (31) subjected to the requirement of zero growth rates up to $t \leqslant 0$ are given by

$$\varsigma_{gJ} = \exp(-i(D\Delta_J)t) \int_0^t v_{gJ}(\tau)\exp(i(D\Delta_J)\tau)\cdot d\tau. \quad (32)$$

From Eq. (32) it is easily inferred that, if $|D\Delta_J|$ values are significantly nonzero for $J=1$ and 2 (as in nonresonant cases), the growth rates v_{gJ} for $\bar{v}(x,t)$ and ς_{gJ} for $\delta'(x,t)$ are of the same order of magnitude. Thus the physical mechanisms inherent in Eq. (27) do not affect these growth rates in any *special* way. However, for $|D\Delta_1| \cong 0$ in Eq. (32), ς_{g1} significantly starts growing as $|\varsigma_{g1}| \cong |\int_0^t v_{g1}(\tau)d\tau| \approx t|v_{g1}(x_c(t),t)|_{av} \geqslant O(\varepsilon \cdot t)$. Therefore by choosing frequency $f_{ext} = f_{ext}(x) \equiv 1/T(x)$ to satisfy the resonance condition $|D\Delta_1| \cong 0$, i.e.,

$$\lambda f_{ext}(x) = \overline{u}(x,t) \cong \overline{u}_{steady}(x) \cong \overline{u}_{mean}(x), \quad (33)$$

one can match the phase speed $\lambda f_{ext}(x)$ of the bottom wall noise to the phase speed $\overline{u}_{steady}(x)$ of the *intrinsic initial disturbance waves*. It should be noted that, even for this case, $|D\Delta_2|$ is nonzero. Indeed, under these conditions, this resonance phenomenon is seen in Fig. 13(*a*). The fact that, in Fig. 13(*a*), interfacial waves' wavelengths only approximately equal wall-noise wavelength λ and $\overline{u}(x,t)$ only approximately equal $\overline{u}_{steady}(x)$ is due to the fact that the amplitude of $\delta'(x,t)$ are not infinitesimal (as was assumed in the above analysis). All else being the same in Fig. 13(*a*), it is clear that the resonant case has significantly more wave energy than the same amplitude non-resonant noise. Thus whenever resonance condition in Eq. (33) is satisfied, the mechanisms represented by Eq. (27) imply that the forward moving component of the noise and the small amplitude *intrinsic interfacial waves* have the same phase speeds and this leads to phase reinforcements and significant increase in the amplitude of δ'.

Although the results shown in Fig. 13 are for a sinusoidal standing wave on the condensing surface at $y=0$, more complex two-dimensional or three-dimensional patterns will arise from a more general noise that would *typically* be present. Furthermore, even if the noise itself is two-dimensional any three-dimensional imperfection in the geometry may cause the wave to become three-dimensional further downstream, and this is perhaps the reason why two-dimensional waves become three-dimensional in some of the known experiments (see, e.g., Lu [21]).

Although it is not presented here, effects of any *general* two-dimensional noise (as measured experimentally by accelerometers) can also be estimated by looking at the power density function of $v_1(x,0,t)$, through FFT, in the k-ω space (wave number $k \equiv 2\pi/\lambda$ and angular frequency $\omega \equiv 2\pi f$) and representing the disturbance $v_1(x,0,t)$ by a representative sum of Fourier components of wavelengths λ and frequencies f.

The CFD simulation restrictions on wavelengths λ that can be investigated is: $\Delta x^*/2 < \lambda < x_e/2$, where Δx^* is of the order of magnitude of the largest x-width in grid A and grid B and x_e is the distance between the inlet and the outlet. The smallest time step Δt^* is the minimum of $(\Delta x/\overline{u})$ values due to Cr$\cong$1 restriction in Eq. (24). This restricts the maximum frequency $f = f_{max}$ that can be computationally studied to those that satisfy the Nyquist criteria $f_{max} < 1/(2\cdot\Delta t^*)$. Despite these restrictions on noise-sensitivity analyses, the *stability* results in Section 5 are true for all wavelengths λ. This is because the resulting interfacial wavelengths are increasing in nature and they increase to a value where it can be resolved by the refined grids employed in this paper.

With regard to noise sources other than the bottom plate noise, it was found that noise or fluctuations in the inlet velocity profile only leads to fluctuations in the vapor profile and has *little* impact on the interfacial waviness. In other words, under unconstrained exit conditions, only fluctuations in flow variables that significantly influence fluctuations in transverse liquid velocity $v_1(x,y,t)$ cause significant interfacial waviness. However, this paper can not account for density fluctuations that necessarily appear in the study of effects of superposed fluctuations in the exit conditions while the inlet conditions are being held fixed.

6 Convergence, Accuracy, and Other Regularities of the Solutions

For a computational solution to be accurate, it needs to satisfy the following criteria: (i) the convergence criteria in the interior of each fluid (i.e., smallness of "b" defined on p. 125 of Patankar [40]), (ii) the satisfaction of all the interface conditions, (iii) grid independent solutions for grids that are sufficiently refined, and (iv) unsteady simulation results for the sensitive interface locations should be free of computational noise in the absence of physical noise. The simulations presented here satisfy all the above criteria.

The satisfaction of the governing equations in the interior and all the conditions at the interface is demonstrated in Liang [2]. For sufficiently refined grid (i.e., both grid A and grid B described in Section 3) and sufficiently large (but not too large) number of

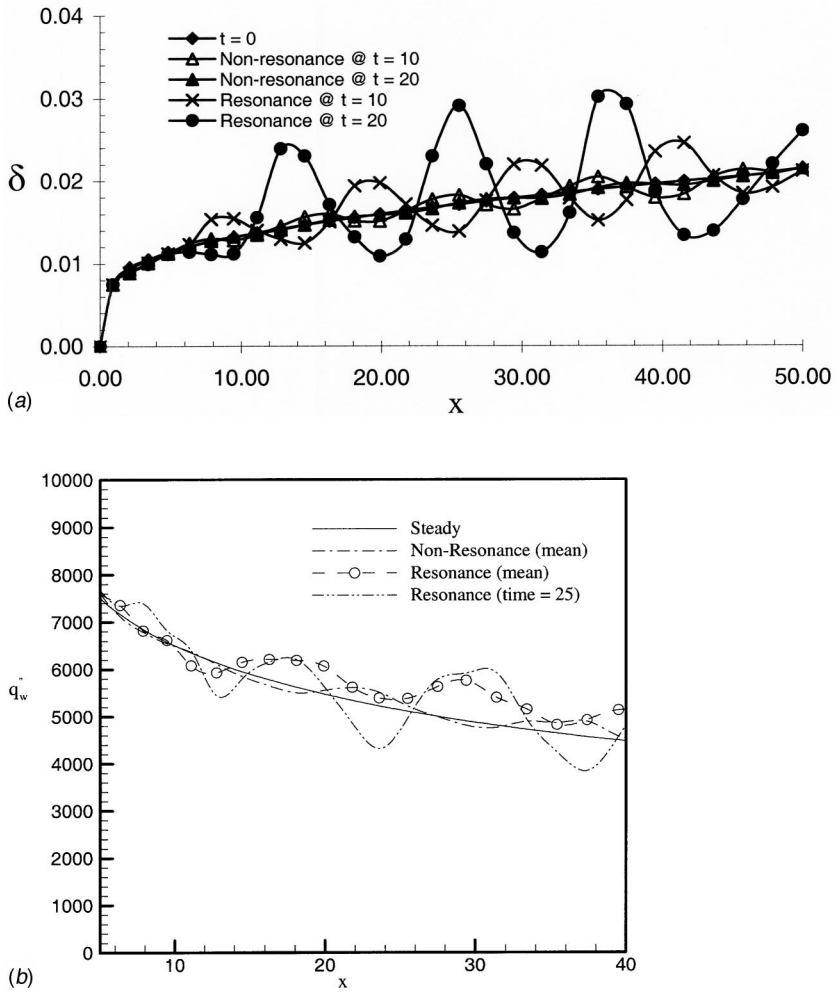

Fig. 13 (*a*) For the flow situations specified in Table 1 with α=90 deg, x_e=50 and Z_e=0.578; the above $\delta(x,t)$ predictions compare the nonresonant noise with a resonant noise of the same amplitude (ε=0.9E-4). The noise is given by: $v_1(x,0,t)=\varepsilon\cdot\sin(2\pi x/\lambda)\cdot\sin(2\pi t/T)$, where (i) λ=10 and T=24 for the nonresonant case, and (ii) λ=10 and $T=T(x)=\lambda/\bar{u}_{\text{steady}}(x)$. (*b*) For the flow situations considered in Fig. 13(*a*), the above depicts the wall heat flux $q''_w(x,t)$, in *W*, at t=25 for the resonant case, and its time-averaged values $\bar{q}''_w(x)$, in *W*, for all other cases.

iterations, the combined sum of decreasing truncation and increasing roundoff errors are minimized to a plateau level and the solutions in Fig. 14(*a*) are grid independent to within 1–2%. The number of grid lines $n_i\times n_j|_L\times n_j|_v$ given in Fig. 14, respectively, indicate the number of grid lines over $0\leqslant x\leqslant x_e$, $0\leqslant y\leqslant\delta_{\text{steady}}(x)$, and $\delta_{\text{steady}}(x)\leqslant y\leqslant 1$ for the interface location at $t=0$. These numbers somewhat change with time. For grid II in Fig. 14(*a*), $(\Delta x)_{av}\equiv x_e/n_i=0.77$, $(\Delta y)_{avL}\equiv\delta(x_e)/n_j|_L=5.77\times10^{-4}$, $(\Delta y)_{avV}\equiv\{1-\delta(x_e)\}/n_j|_v=0.015$, and $\Delta t=5$. The corresponding representative grid spacing values in physical variables are $(\Delta x)_{av}=3.08$ mm, $(\Delta y)_{avL}=2.31$ μm, $(\Delta y)_{avV}=0.06$ mm, and $\Delta t=0.049$ s. For a technical estimate of total discretization error—Section 3.10 in Ferziger and Peric [41] is used for estimating error on a representative flow variable (say, film thickness in Fig. 14(*b*)) due to the coarseness of *x*-grid. On successive refinement of the *x*-grid, the results in Fig. 14(*b*) yield the error to be within 3%. Considering this and the refinement used in the time and in the *y*-direction, the total error of all reported results in this paper is about 6%.

Smooth interface unsteady solutions reported earlier in Fig. 8(*a*) establish that the highly sensitive interface predictions are free of computational noise whenever there is an absence of physical noise. In fact, in Liang [2], it is shown that inappropriate discretization schemes for the interface tracking equation or unsuitable choice of splines for mapping variable values between grid A and grid B can lead to wavy interface solutions even in the absence of physical noise. Such waves that are entirely due to computational noise have been eliminated from the present study.

Another regularity of the proposed computational approach is its ability to make steady predictions for the classical Nusselt [5] problem in agreement with its classical solution while allowing for improvements in it. This is shown in Fig. 15. The unsteady predictions for this classical problem will be discussed in a separate paper.

7 Trends of the Steady, Stable and Noise-Sensitive Solutions

The steady and stable solution (associated with $Z_e=Z_e|_{\text{Na}}$) in Fig. 8 for the vertical-channel case was found to be sensitive to noise in Fig. 13. Despite the waves, as seen in Fig. 13(*b*), there are no significant enhancements in heat transfer rates for the nonresonant case. This is because the oscillations around the mean film thickness are small and nearly symmetric, and temperature pro-

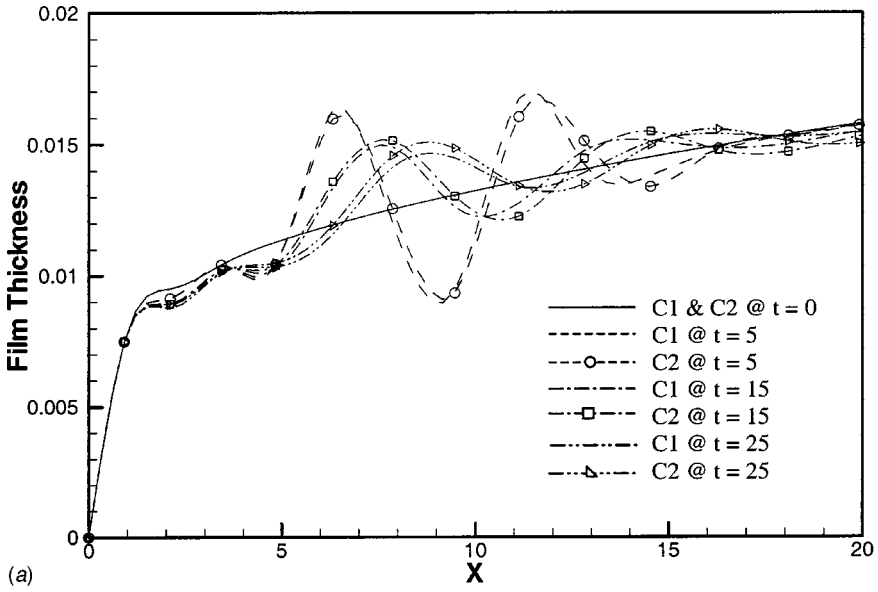

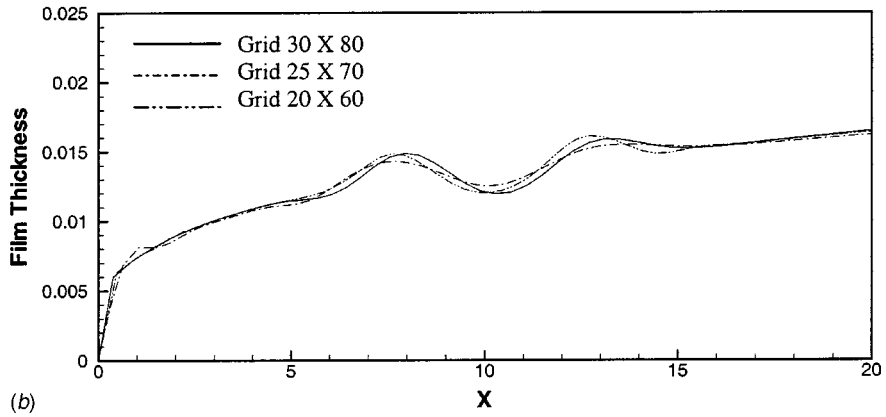

Fig. 14 (*a*) The above $\delta(x,t)$ predictions for $t>0$ are for the steady solution curve $C1=C2$ at $t=0$ and initial noise specified in Fig. 10. The $t=0$ solutions are obtained on two grids I and II with $(n_i\times n_{j|L}\times n_{j|V})_I=(30\times30\times20)$ and $(n_i\times n_{j|L}\times n_{j|V})_{II}=(50\times50\times30)$. The $t>0$ solution are shown as curves $C1$ and $C2$ and are, respectively, obtained on grids that have: $(n_i\times n_{j|L}\times n_{j|V})_I\times\Delta t=(30\times30\times20)\times2.5$ and $(n_i\times n_{j|L}\times n_{j|V})_{II}\times\Delta t=(50\times50\times30)\times5$. At $t>0$, the number of grid lines $(n_i\times n_{j|L}\times n_{j|V})$ changes somewhat from their value at $t=0$.

files are nearly linear. This yields heat flux $q''_w(x,t)\sim\Delta T/\delta(x,t)$ whose time-averaged values show no significant enhancement unless the wave amplitudes are large. As a result, for the larger amplitude resonant case in Fig. 13, there is a significant heat transfer enhancement of 10% or more in the downstream half of the channel. Therefore these stable and quasi-steady $Z_e=Z_e|_{\mathrm{Na}}$ solutions obtained in Fig. 8 are important in their own right for the purpose of estimating *typical* heat flux values. Hence it is good to ascertain the trends of these *natural* steady solutions as the inlet Reynolds number Re_{in} and the temperature difference $\Delta\mathcal{T}$ (or, equivalently, the parameter Ja) are changed. Figure 16 shows the effect of these changes on $Z_e=Z_e|_{\mathrm{Na}}$, Fig. 17 shows the effects on wall heat flux $\overline{q}''_w(x)$, and Fig. 18 shows the effects on flow fields ($\delta_{\mathrm{steady}}(x)$, etc.). Since the vertical channel configuration studied here is gravity-dominated, vapor motion does not significantly affect the condensate motion and, as expected, changes in inlet Reynolds number Re_{in} has no effects on mean film thickness $\delta_{\mathrm{steady}}(x)$ or wall heat flux $\overline{q}''_w(x)$. However, in Fig. 18, a thickening of $\delta_{\mathrm{steady}}(x)$ occurs due to an increase in temperature differ-

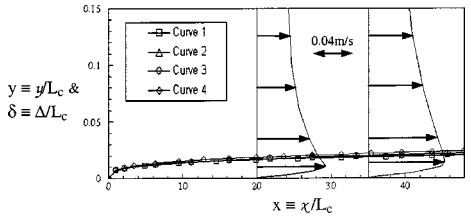

Fig. 15 For the vertical plate situation specified in Table 1 with $\alpha=90$ deg, $x_e=48$ and $L_c=0.004$ m, Curve 1 is a plot of the analytical solution of $\delta(x)$ as given in Nusselt [5]. Curve 2 is the computational solution under the Nusselt assumption for stagnant vapor and zero liquid inertia. Curve 3 is the computational solution under the assumptions of stagnant vapor while allowing for liquid inertia. Curve 4 is the computational solution that allows vapor motion and liquid inertia (the vapor/liquid velocity profiles are shown only for this case). Though not shown above, vapor velocity tends to zero as $y\rightarrow\infty$.

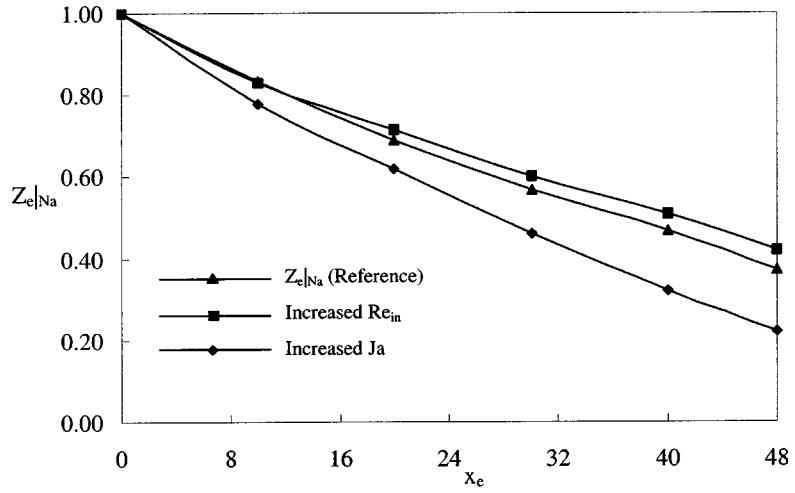

Fig. 16 The above is a plot of natural values of $Z_{e|Na}$ for different x_e values for a representative flow situation specified in Table 1 with α=90 deg and x_e=48. The "Increased Re_{in}" case just changes Re_{in} to a new value of 1300. The "Increased Ja" case just changes Ja to a new value of 0.0443 (i.e., ΔT =65°C).

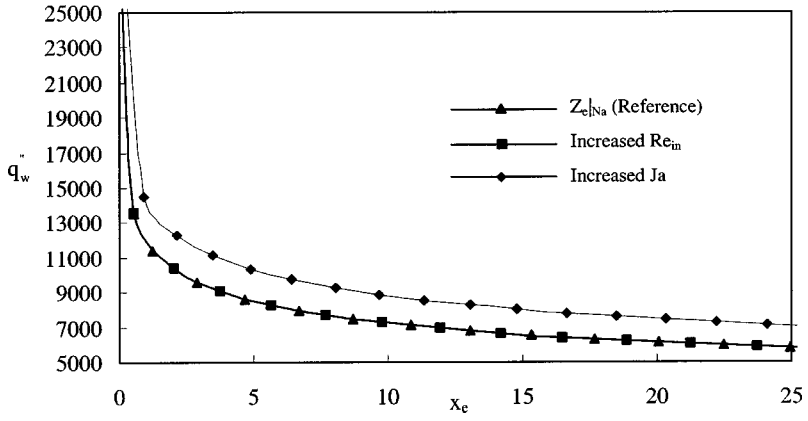

Fig. 17 For the flow situations described in Fig. 16 and x_e=25.0, the above figure reports the representative wall heat flux values $q''_w(x)$, in W, as a function of x with $0 \leq x \leq x_e$

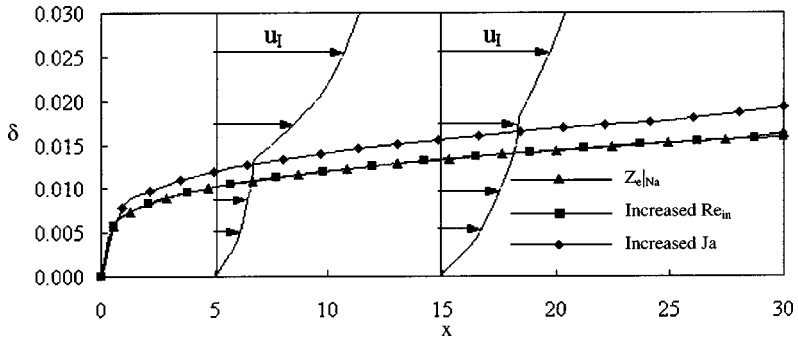

Fig. 18 For the flow situations described in Figs. 16–17 and x_e=30.0, the above figure reports the values of $\delta_{steady}(x)$

ence $\Delta\mathcal{T}$. This thickening occurs in a way so as to concurrently meet the requirements of increased heat flux values (see Fig. 17) and increased liquid flow rates.

Streamline patterns for the flow, effect of shear over gravity as tilt angle α is reduced from its 90 deg value, comparisons with experimental results for condensing flow simulations for a horizontal channel, effects of surface tension, effects of microgravity, negligible Marangoni effects, effects of fluctuations on the mean, etc., are not discussed here but are reported in Liang et al. [1].

8 Conclusions

- An algorithm for a successful computational approach capable of accurate simulation of unsteady wavy interface condensing flows has been presented.
- The "ellipticity" of the steady vapor flow equations and the role of exit conditions for steady and unsteady simulations have been discussed.
- For unconstrained exit conditions and nearly incompressible vapor flows, an unsteady noise-free simulation method for identifying and obtaining the *natural* and *stable* steady solutions has been presented and successfully used.
- The noise sensitivity of the *stable* steady or quasi-steady solutions to ubiquitous minuscule bottom plate vibrations has been demonstrated. To assist in quantitative noise-sensitivity studies, a method for obtaining the underlying *characteristics curves* and estimating "growth/damping" factors for interfacial disturbances has been presented.
- For design of smart condensers with actuators imbedded on the condensing surface, a new and hitherto unknown resonance condition has been proposed, and its efficacy in enhancing wave energy and heat transfer rates (up to 10% or more) has been demonstrated.
- For unconstrained exit situations, some trends of the *stable* steady or quasi-steady solutions have been discussed.

Acknowledgment

This work was partially supported by the NSF grant CTS-0086988.

Appendix

The interface conditions that apply at $\mathcal{H}(x,y,t)=y-\Delta(x,t)=0$, involve values of flow variables at the interface that are denoted by a superscript "*i*." The unit normal at any point on the interface, directed from the liquid towards the vapor, is denoted by $\hat{\mathbf{n}}$ and is equal to $\nabla\mathcal{H}/|\nabla\mathcal{H}|$. The unit tangent at any point on the interface, directed towards increasing x, is denoted by $\hat{\mathbf{t}}$. Each phase is modeled as a viscous and incompressible Newtonian fluid with stress tensor $\mathbf{T}=-p_I\mathbf{1}+\mathbf{S}_I$ where $\mathbf{S}_I=\mu_I\{(\text{grad}\cdot\mathbf{v}_I)+(\text{grad}\cdot\mathbf{v}_I)^T\}/2$ and $\mathbf{1}$ is the identity tensor.

- The surface velocity $\mathbf{v}_s^i$ of a point on the interface ($\mathcal{H}=0$) at time t is associated with this point's movement to a new mapped position on the interface at time $t+\Delta t$. All such mappings must be such that the normal component of this $\mathbf{v}_s^i$ is given by

$$\mathbf{v}_s^i\cdot\hat{\mathbf{n}}=-(\partial\mathcal{H}/\partial t)/|\nabla\mathcal{H}|. \tag{A1}$$

- The tangential component of the vapor and liquid velocities at the interface must be continuous, i.e.,

$$\mathbf{v}_1^i\cdot\hat{\mathbf{t}}=\mathbf{v}_2^i\cdot\hat{\mathbf{t}}. \tag{A2}$$

- Ignoring normal component of $\nabla_s\sigma$ and viscous stresses, the normal component of momentum balance at a point on the interface is given by

$$\begin{aligned}p_1^i&=p_2^i+\dot{m}^2(1/\rho_2-1/\rho_1)+\sigma\nabla_s\cdot\hat{\mathbf{n}}-\nabla_s\sigma\cdot\hat{\mathbf{n}}+(\mathbf{S}_1^i-\mathbf{S}_2^i)\hat{\mathbf{n}}\cdot\hat{\mathbf{n}}\\&\cong p_2^i+\dot{m}^2(1/\rho_2-1/\rho_1)-(\sigma\Delta_{xx})/[1+\Delta_x^2]^{2/3}.\end{aligned} \tag{A3}$$

- The tangential component of momentum balance at any point on the interface, for nearly constant surface tension σ, reduces to

$$\mathbf{S}_1^i\hat{\mathbf{n}}\cdot\hat{\mathbf{t}}=\mathbf{S}_2^i\hat{\mathbf{n}}\cdot\hat{\mathbf{t}}+\nabla_s\sigma\cdot\hat{\mathbf{t}}\cong\mathbf{S}_2^i\hat{\mathbf{n}}\cdot\hat{\mathbf{t}}. \tag{A4}$$

- The mass fluxes $\dot{m}_{VK}$ and $\dot{m}_{LK}$ as determined by kinematic restrictions imposed by interfacial values of vapor and liquid velocities are

$$\dot{m}_{VK}\equiv-\rho_2(\mathbf{v}_2^i-\mathbf{v}_s^i)\cdot\hat{\mathbf{n}}\ \text{ and }\ \dot{m}_{LK}\equiv-\rho_1(\mathbf{v}_1^i-\mathbf{v}_s^i)\cdot\hat{\mathbf{n}}. \tag{A5}$$

- The energy balance at a point on the interface imposes a restriction on the interfacial mass flux $\dot{m}_{\text{Energy}}$, and this is given by

$$\begin{aligned}\dot{m}_{\text{Energy}}=1/h_{fg}\Bigg[&\{k_1\nabla\mathcal{T}_1|^i\cdot\hat{\mathbf{n}}-k_2\nabla\mathcal{T}_2|^i\cdot\hat{\mathbf{n}}\}+\frac{d\sigma}{dt}\Big|_s\\&+\frac{1}{2}\dot{m}\{|\mathbf{v}_1^i-\mathbf{v}_s^i|^2-|\mathbf{v}_2^i-\mathbf{v}_s^i|^2\}\\&+\{\mathbf{S}_1^i\hat{\mathbf{n}}\cdot(\mathbf{v}_1^i-\mathbf{v}_s^i)-\mathbf{S}_2^i\hat{\mathbf{n}}\cdot(\mathbf{v}_2^i-\mathbf{v}_s^i)\}\Bigg]\\\cong 1/h_{fg}\Bigg[&k_1\frac{\partial\mathcal{T}_1}{\partial n}\Big|^i-k_2\frac{\partial\mathcal{T}_2}{\partial n}\Big|^i\Bigg].\end{aligned} \tag{A6}$$

- Mass balance at any point on the interface requires single valuedness of the interfacial mass flux. That is

$$\dot{m}_{LK}=\dot{m}_{VK}=\dot{m}_{\text{Energy}}\equiv\dot{m}. \tag{A7}$$

- To account for the effects of nonzero interfacial mass flux $\dot{m}$, the interfacial pressures p_1^i and p_2^i (along with their difference $\Delta p^i\equiv p_1^i-p_2^i$) that appear in Eq. (*A*3) are often considered to be controlled by nonequilibrium thermodynamic effects that are represented by the functions: $p_1^i\equiv p_{1\,n\text{-}eq}^i(\mathcal{T}_1^i)$ and $p_2^i\equiv p_{2\,n\text{-}eq}^i(\mathcal{T}_2^i)$, where $\mathcal{T}_1^i$ is the liquid side interfacial temperature and $\mathcal{T}_2^i$ is the vapor side interfacial temperature. In the limit of zero mass flux $\dot{m}$, these thermodynamic pressures reach their equilibrium thermodynamic values and are denoted as $p_1^i\equiv p_{\text{sat}}(\mathcal{T}_1^i)$ and $p_2^i\equiv p_{\text{sat}}(\mathcal{T}_2^i)$, where p_{sat} is the inverse function of the saturation temperature $\mathcal{T}_s(p)$. Respectively denoting the non-equilibrium and equilibrium values of the interfacial pressure differences as $(\Delta p^i)_{n\text{-}eq}$ and $(\Delta p^i)_{\text{sat}}$, it is common to *seek* or *model* a function f such that $(\Delta p^i)_{n\text{-}eq}=f\{(\Delta p^i)_{\text{sat}},\dot{m}\}$, where f, be it *explicit* or *implicit* in form, allows the two pressure differences to become the same for zero mass flux $\dot{m}$. It is common to *model* f by considerations (see, e.g., Plesset and Prosperetti [44] and Section 4.5 of Carey [37]) involving kinetic theory of gas for the vapor phase, the concept of accommodation coefficients, etc. The assumption that use of either $(\Delta p^i)_{n\text{-}eq}$ or $(\Delta p^i)_{\text{sat}}$ do not significantly affect the value of $\Delta\mathcal{T}^i\equiv\mathcal{T}_s(p_2^i+\Delta p^i)-\mathcal{T}_s(p_2^i)$ is well known and well justified in the present context where significantly larger thermal resistance is offered by the thin condensate at points away from $x\sim 0$ (see Section 4.5 of Carey [37] and Son and Dhir [22]). Furthermore, the computations in this paper also show that the solution further downstream is not affected by the nature of the singular solution at $x\sim 0$ and computed values in this zone always satisfy $\Delta\mathcal{T}^i\equiv\mathcal{T}_s(p_2^i+\Delta p^i)-\mathcal{T}_s(p_2^i)\cong 0$— in the sense that $\Delta\mathcal{T}^i\ll\Delta\mathcal{T}$, where $\Delta\mathcal{T}$ is the number defined in Eq. (1). Therefore, under negligible interfacial resistance approximation, the interfacial temperature values satisfy:

$$\mathcal{T}_1^i\cong\mathcal{T}_2^i=\mathcal{T}_s(p_2^i). \tag{A8}$$

- The term $[t]$ on the right side of Eq. (5) is given by

$$[t]=\left\{\frac{\mu_2}{\mu_1}\frac{\partial v_2}{\partial x}\bigg|^i-\frac{\partial v_1}{\partial x}\bigg|^i\right\}+\frac{2\delta_x}{[1-\delta_x^2]}\left\{\frac{\partial u_1}{\partial x}\bigg|^i-\frac{\partial v_1}{\partial y}\bigg|^i\right\}$$
$$-\frac{2\delta_x}{[1-\delta_x^2]}\frac{\mu_2}{\mu_1}\left\{\frac{\partial u_2}{\partial x}\bigg|^i-\frac{\partial v_2}{\partial y}\bigg|^i\right\}. \quad (A9)$$

References

[1] Liang, Q., Wang, X., and Narain, A., 2004, ''Effects of Gravity, Shear, and Surface Tension in Internal Condensing Flows—Results from Direct Computational Simulations,'' (accepted for publication in the ASME *Journal of Heat Transfer*).

[2] Liang, Q., 2003, ''Unsteady Computational Simulations and Code Development for a Study of Internal Film Condensation Flows' Stability, Noise-Sensitivity, and Waviness,'' Ph.D. thesis, Michigan Technological University.

[3] Krotiuk, W. J., 1990, *Thermal-Hydraulics for Space Power, Propulsion, and Thermal Management System Design*, American Institute of Aeronautics and Aeronautics, Washington, DC.

[4] Faghri, A., 1995, *Heat Pipe Science and Technology*, Taylor and Francis, Washington, DC.

[5] Nusselt, W., 1916, ''Die Oberflächenkondesation des Wasserdampfes,'' Z. Ver. Dt. Ing., **60**(27), pp. 541–546.

[6] Rohsenow, W. M., 1956, Heat Transfer and Temperature Distribution in Laminar Film Condensation, Trans. ASME, **78**, pp. 1645–1648.

[7] Sparrow, E. M., and Gregg, J. L., 1959, ''A Boundary Layer Treatment of Laminar Film Condensation,'' ASME J. Heat Transfer, **81**, pp. 13–18.

[8] Koh, J. C. Y., Sparrow, E. M., and Hartnett, J. P., 1961, ''The Two-Phase ry Layer in Laminar Film Condensation,'' Int. J. Heat Mass Transfer, **2**, pp. 69–82.

[9] Dhir, V. K., and Lienhard, J. H., 1971, ''Laminar Film Condensation on Plane and Axisymmetric Bodies in Nonuniform Gravity,'' ASME J. Heat Transfer, **93**, pp. 97–100.

[10] Rose, J. W., 1988, ''Fundamentals of Condensation Heat Transfer: Laminar Film Condensation,'' JSME Int. J., **31**, pp. 357–375.

[11] Tanasawa, I., 1991, ''Advances in Condensation Heat Transfer,'' Adv. Heat Transfer, **21**, pp. 55–131.

[12] Cess, R. D., 1960, ''Laminar Film Condensation on a Flat Plate in the Absence of a Body Force,'' ZAMP, **11**, pp. 426–433.

[13] Koh, J. C. Y., 1962, ''Film Condensation in a Forced Convection Boundary Layer Flow,'' Int. J. Heat Mass Transfer, **5**, pp. 941–954.

[14] Kutateladze, S. S., 1963, *Fundamentals of Heat Transfer*, Academic Press, San Diego, CA.

[15] Labuntsov, D. A., 1957, ''Heat Transfer in Film Condensation of Pure Steam on Vertical Surfaces and Horizontal Tubes,'' Teploenergetica, **4**, p. 72. Also see (in Russian) ''Heat Transfer During Condensation of Steam on a Vertical Surface in Conditions of Turbulent Flow of a Condensate Film,'' 1960, Inghenerno-Fizicheski Zhurnal, **3**, pp. 3–12.

[16] Incropera, F. P., and DeWitt, D. P., 1996, *Fundamentals of Heat and Mass Transfer*, 4th Ed., John Wiley and Sons, New York.

[17] Yu, G., 1999, ''Development of a CFD Code for Computational Simulations and Flow Physics of Annular/Stratified Film Condensation Flows,'' *Ph.D. thesis*, ME-EM Department, Michigan Technological University.

[18] Chow, L. C., and Parish, R. C., 1986, ''Condensation Heat Transfer in Microgravity Environment,'' *Proceedings of the 24th Aerospace Science Meeting*, AIAA, New York.

[19] Narain, A., Yu, G., and Liu, Q., 1997, ''Interfacial Shear Models and Their Required Asymptotic Form for Annular/Stratified Film Condensation Flows in Inclined Channels and Vertical Pipes,'' Int. J. Heat Mass Transfer, **40**(15), pp. 3559–3575.

[20] Henstock, W. H., and Hanratty, T. J., 1976, ''The Interfacial Drag and the Height of the Wall Layer in Annular Flows,'' AIChE J., **22**, pp. 990–1000.

[21] Lu, Q., 1992, ''An Experimental Study of Condensation Heat Transfer With Film Condensation in a Horizontal Rectangular Duct,'' *Ph.D. thesis*, Michigan Technological University.

[22] Sussman, M., Smereka, P., and Osher, S., 1994, ''A Level Set Approach for Computing Solutions to Incompressible Two-Phase Flow,'' J. Comput. Phys., **114**, pp. 146–159.

[23] Son, G., and Dhir, V. K., 1998, ''Numerical Simulation of Film Boiling Near Critical Pressures with a Level Set Method,'' ASME J. Heat Transfer, **120**, pp. 183–192.

[24] Hirt, C. W., and Nichols, B. D., 1981, ''Volume of Fluid (VOF) Method for the Dynamics of Free Boundaries,'' J. Comput. Phys., **39**, pp. 201–255.

[25] Tezduyar, T. E., 2001, ''Finite Element Interface-Tracking and Interface-Capturing Techniques for Flows with Moving Boundaries and Interfaces,'' *Proceedings of the ASME Symposium on Fluid Physics and Heat Transfer for Macro and Micro-Scale Gas-Liquid and Phase-Change Flows*, HTD-Vol. 369-3, ASME, New York.

[26] Abbott, M. B., and Basco, D. R., 1989, *Computational Fluid Dynamics—An Introduction For Engineers*, Longman, pp. 86–88, Ch. 3, pp. 151–155, Ch. 5.

[27] Li, J., and Renardy, Y., 2000, ''Numerical Study of Flows of Two Immiscible Liquids at Low Reynolds Number,'' SIAM Rev., **42**(3), pp. 417–439.

[28] Lu, Q., and Suryanarayana, N. V., 1995, ''Condensation of a Vapor Flowing Inside a Horizontal Rectangular Duct,'' ASME J. Heat Transfer, **117**, pp. 418–424.

[29] Bhatt, B. L., Wedekind, G. L., and Jung, K., 1989, ''Effects of Two-Phase Pressure Drop on the Self-Sustained Oscillatory Instability in Condensing Flows,'' ASME J. Heat Transfer, **111**, pp. 538–545.

[30] Liu, J., and Gollub, J. P., 1994, ''Solitary Wave Dynamics of Film Flows,'' Phys. Fluids, **6**(5), pp. 1702–1712.

[31] Alekseenko, S. V., Nakoryakov, V. E., and Pokusaev, B. G., 1994, *Wave Flow of Liquid Films*, Begell House, New York.

[32] Miyara, A., 2001, ''Flow Dynamics and Heat Transfer of Wavy Condensate Film,'' ASME J. Heat Transfer, **123**, pp. 492–500.

[33] Lighthill, J., 1979, *Waves in Fluids*, Cambridge University Press, Cambridge, UK.

[34] Traviss, D. P., Rohsenow, W. M., and Baron, A. B., 1973, ''Forced Convection Condensation Inside Tubes: A Heat Transfer Equation for Condenser Design,'' ASHRAE Trans., **79**, Part 1, pp. 157–165.

[35] Shah, M. M., 1979, ''A General Correlation for Heat Transfer during Film Condensation inside Pipes,'' Int. J. Heat Mass Transfer, **22**, pp. 547–556.

[36] Hewitt, G. F., Shires, G. L., and Polezhaev, Y. V., eds., 1997, *International Encyclopedia of Heat and Mass Transfer*, CRC Press, Boca Raton, FL.

[37] Carey, V. P., 1992, *Liquid-Vapor Phase-Change Phenomena*, Series in Chemical and Mechanical Engineering, Hemisphere, Washington, DC.

[38] Palen, J. W., Kistler, R. S., and Frank Y. Z., 1993, ''What We Still Don't Know About Condensation in Tubes,'' *Condensation and Condenser Design* J. Taborek, J. Rose, and I. Tanasawa, eds., United Engineering Trustees, Inc. for Engineering Foundation and ASME, New York, pp. 19–53.

[39] Delhaye, J. M., 1974, ''Jump Conditions and Entropy Sources in Two Phase Systems: Local Instant Formulation,'' Int. J. Multiphase Flow, **1**, pp. 395–409.

[40] Patankar, S. V., 1980, *Numerical Heat Transfer and Fluid Flow*, Hemisphere, Washington DC.

[41] Ferziger, J. H., and Peric, M., 1997, *Computational Methods for Fluid Dynamics*, Springer, Berlin.

[42] Greenberg, M. D., 1978, *Foundations of Applied Mathematics*, Prentice-Hall, Englewood Cliffs, Jersey.

[43] Joseph, D. D., 1976, *Stability of Fluid Motions*, Vol. 1, Springer-Verlag, New York, pp. 7–8.

[44] Plesset, M. S., and Prosperetti, A., 1976, ''Flow of Vapor in a Liquid Enclosure,'' J. Fluid Mech., **78**(3), pp. 433–444.

[45] *ASHRAE Handbook*, 1985, Fundamentals SI Edition, American Society of Heating, Refrigeration and Air-Conditioning Engineers, Atlanta, GA.